



The  
University  
Of  
Sheffield.

Department of Automatic Control  
& Systems Engineering

Design of an Actively Controlled  
Mechanical Metamaterial with  
Simultaneously Negative Density  
and Elastic Modulus

ACS420 MEng Advanced Project May 2017

Theodore Abbott - 120139831  
Supervised by Dr Simon Pope

A dissertation submitted in partial fulfilment of the requirements for  
the degree of Master of Engineering in Systems and Control.

## **Executive Summary**

Metamaterials have potential applications in superlenses and cloaking, given their current low technology readiness level more applications will likely be found as the field develops. Cloaking has a myriad of uses such as allowing submarines to become invisible to sonar, defence of the foundations of buildings from earthquakes and isolation of sensitive equipment from vibration.

This project has built on previous work to produce a hardware design capable of displaying the needed properties (negative effective mass and stiffness) in one and two dimensions. A model and control algorithms have been derived and one of the needed properties has been experimentally demonstrated. As far as the author is aware, the hardware produced is the most compact ever constructed within the field of structural mechanical metamaterials.

## Abstract

All known conventional materials have positive refractive index. According to Snell's law this results in incident waves being refracted to the opposite side of the normal line. Veselago (1967) was the first to theorise on the properties required to exhibit negative refractive index to incident electromagnetic waves. Materials with this property have possible applications in areas such as superlenses and invisibility cloaks.

Recently analogous acoustic and elastic metamaterials have been developed that are able to produce negative refraction within a frequency band. This behaviour requires the material have simultaneously negative effective density and stiffness at the frequency of interest. While both passive and active metamaterials have been demonstrated, the latter possess a significant advantage due to the inherent flexibility of rapid tunability and potential for broadband operation. Current limitations on this work are the width of the double negative frequency band, scale and lack of dimensionality.

The purpose of this project is to miniaturise previous work while increasing the double negative bandwidth. The hardware produced will allow the metamaterial to have a negative refractive index in one and two dimensions. Control algorithms for double negativity have been developed and the mass control algorithm was implemented on the hardware giving the expected result in one dimension.

Acoustic metamaterials have potential applications in the area of acoustic cloaking such as required to prevent detection of submarines by sonar. Vibrational cloaking may be used to defend the foundations of buildings from earthquakes. Sensitive equipment may be isolated from vibration such as sensors in engines. Metamaterials, particularly mechanical metamaterials currently have a low technology readiness level, as such more applications will likely be found as the field develops.

## **Acknowledgements**

First I must thank the staff within the ACSE department which has been a home away from home for the past four years. More specifically my gratitude goes to Linda Grey, Bryn Jones and the many others who are too numerous to list here.

My gratitude goes to Craig Bacon, Anthony Whelpton and Jack Powell for their advice during the design of the hardware and their support with LabVIEW. I would also like to thank Wendy Birtwistle and Kurt Bonser from the AdAM Centre for the use of their equipment and help while printing NinjaFlex.

I would like to thank my supervisor, Dr Simon Pope, without his consistent clarity of thought, and ability to communicate challenging ideas, it would have taken much longer to achieve far less.

Finally, I must thank my parents and my brothers whom I appreciate more than they know.

# Contents

<b>1</b>	<b>Introduction</b>	<b>1</b>
1.1	Project Background . . . . .	1
1.2	Acoustic and Elastic Metamaterials . . . . .	3
1.3	Actively Controlled Metamaterials . . . . .	4
1.4	Motivation . . . . .	6
1.5	Initial Design . . . . .	7
1.6	Project Aim and Objectives . . . . .	8
1.6.1	Aim . . . . .	8
1.6.2	Basic Objectives . . . . .	8
1.6.3	Advanced Objectives . . . . .	8
1.6.4	Objectives Beyond the State of the Art . . . . .	8
1.7	Project Management . . . . .	9
1.7.1	Resources . . . . .	9
1.7.2	Risks . . . . .	9
1.7.3	Risk Management . . . . .	9
<b>2</b>	<b>Modelling and Simulation</b>	<b>10</b>
2.1	Modelling Simplifications . . . . .	11
2.2	Notation . . . . .	12
2.3	Passive Transmission and Actuator Mass System . . . . .	13
2.3.1	Modelling . . . . .	13
2.3.2	Simulation . . . . .	14
2.4	Control Forces . . . . .	15
2.5	Actively Controlled System . . . . .	16
2.5.1	Modelling . . . . .	16
2.5.2	Actuator Dynamics . . . . .	17
2.5.3	Simulation . . . . .	18
<b>3</b>	<b>Hardware Design</b>	<b>19</b>
3.1	Design Objectives . . . . .	19
3.2	Cell Topology . . . . .	19
3.3	Input/Output and Control . . . . .	20
3.4	Actuation . . . . .	20
3.4.1	Actuation . . . . .	20
3.4.2	Circuit Design . . . . .	20

3.5	Sensing . . . . .	21
3.5.1	Acceleration . . . . .	21
3.5.2	Disturbing LRA Force . . . . .	22
3.5.3	Circuit Design . . . . .	22
3.6	Transmission Mass Body . . . . .	24
3.6.1	Material . . . . .	24
3.6.2	Form . . . . .	26
3.6.3	Manufacturing . . . . .	27
3.7	Spring Element . . . . .	28
3.7.1	Design . . . . .	28
3.7.2	Manufacturing . . . . .	29
3.8	Transmission Mass Body Redesign . . . . .	32
3.8.1	Simulation . . . . .	34
3.8.2	Single Cell Assembly . . . . .	34
3.9	PTFE Surface Plate . . . . .	35
3.10	Full Assembly . . . . .	36
3.11	Simulation of Design . . . . .	37
<b>4</b>	<b>Implementation, Results and Analysis</b>	<b>40</b>
4.1	National Instruments LabVIEW . . . . .	40
4.2	Sampling . . . . .	40
4.3	Test Setup . . . . .	42
4.4	Data Processing and Results . . . . .	43
4.4.1	Passive System . . . . .	43
4.4.2	Active System . . . . .	46
<b>5</b>	<b>Conclusion</b>	<b>49</b>
5.1	Future Work . . . . .	49
5.2	Progress Against Aim and Objectives . . . . .	50
5.2.1	Aim . . . . .	50
5.2.2	Basic Objectives . . . . .	50
5.2.3	Advanced Objectives . . . . .	51
5.3	Project Management . . . . .	51
<b>6</b>	<b>Appendices</b>	
6.1	Appendix A: MATLAB code used to simulate effective mass and stiffness. . .	
6.2	Appendix B: LabVIEW code used to for experimental mass control. . . . .	
6.3	Appendix C: LabVIEW code used to for experimental mass and stiffness control.	
6.4	Appendix D: Progress Report 1 . . . . .	
6.5	Appendix D: Progress Report 2 . . . . .	

# Chapter 1

## Introduction

### 1.1 Project Background

The prefix ‘meta’ translates from the Greek ‘beyond’, metamaterials are therefore a class of materials displaying properties outside those typically found in conventional materials. In 1967 Veselago wrote the first theoretical description of a material with negative permeability and permittivity (ability to support internal magnetic fields and internal electric fields respectively). He called these double negative materials ‘left-handed’, and theorised on novel properties such a material would have:

1. Radiation travelling through the material would exhibit negative group velocity while retaining positive phase velocity (velocities are anti-parallel) causing novel physical effects such as reversed Doppler and Vavilov-Cherenkov effects.
2. Negative refractive index; an electromagnetic ray travelling into a left-handed material would be refracted on the opposite side of the normal as is usually expected (Figure 1.1).
3. A photon propagating through a left-handed material, when reflected off an object, would impart momentum in the opposite direction to what is expected. In other words, shining a light on an object through a left-handed medium will pull it toward the light rather than a push it away. Shelby (2001) later described this as negative radiation pressure.

Pendry (2000) continued the work of Veselago exploring the usefulness of negative refractive index for superlenses (lenses capable of focusing light onto an area smaller than a square with sides equal to the wavelength of the light being focused). These lenses would not be concave or convex, rather they would have a slab shaped design and would not focus incident light from infinity, instead refocusing light from a finite distance away.

In other work Pendry (1999) gave designs for a structure made from a non-magnetic material which displayed effective magnetic permeability when exposed to microwaves (1 to 1000 mm), this was achieved by exploiting the resonant properties of split ring resonators. This work was developed by Smith (2000) who gave a theoretical description of how both negative permittivity and permeability could be achieved using the same design. In simula-

tion, Smith was able to produce negative permeability over a bandwidth of 400MHz between 4.2GHz and 4.6GHz; limited experiments were also conducted demonstrating the double negative behaviour, though with lower bandwidth. Shelby (2001) experimentally validated the double negative behaviour and noted that split ring resonators are unlikely to produce this behaviour across the visible spectrum (430 to 770 THz) due to scaling issues. The common limitation for visible spectrum light manipulation is the wavelength of light, this is because the structure of the metamaterial must be homogeneous when viewed at the scale of the wave being manipulated. Green light has a wavelength of 510 nm requiring fabrication on the nanoscale. Gralak (2000) suggests though theoretical analysis that photonic crystals may overcome this limitation producing similar behaviour at the scales required for visible light. Alternative designs close to the the visible spectra include plasmonic parallel nano-wires (Podolskiy 2002) and the inclusion of sub-wavelength rings of plasmonic nanoparticles which display magnetic dipole behaviour (A. Alu 2006).

Photonic metamaterials have potential applications in areas such as superlenses and invisibility cloaks. It is important to clarify that these materials should not display a high level of energy absorption for either of these applications, in fact high absorption would disqualify them from these uses. Vertically aligned carbon nanotube arrays (VANTAs) display exceptionally high absorption of incident visible light with only 0.036% being reflected and the remainder absorbed (Theocharous 2014); however, the lack of reflected light makes the location of an object with this coating obvious, except for when the background of the object contains no photon source or reflective objects. In order for effective cloaking the incident light must pass through or around the material so that objects behind (relative to the viewer) the device being cloaked are visible. Additionally, reflection of incident rays should be minimised requiring matching of the refractive indices.

Figure 1.1 shows the path of light moving between materials with both positive and negative refractive indices. In both cases the refraction is governed by Snell's law:  $n_1 \sin \theta_1 = n_2 \sin \theta_2$ . The refractive index  $n$  is defined as the ratio of the speed of light. The refractive index  $n$  of an optical medium is defined as the ratio of the speed of light in vacuo to the phase velocity  $v$  of light in the medium  $n = \frac{c}{v}$ . Materials achieving negative refractive index display negative phase velocity causing  $\frac{c}{v}$  to become negative.

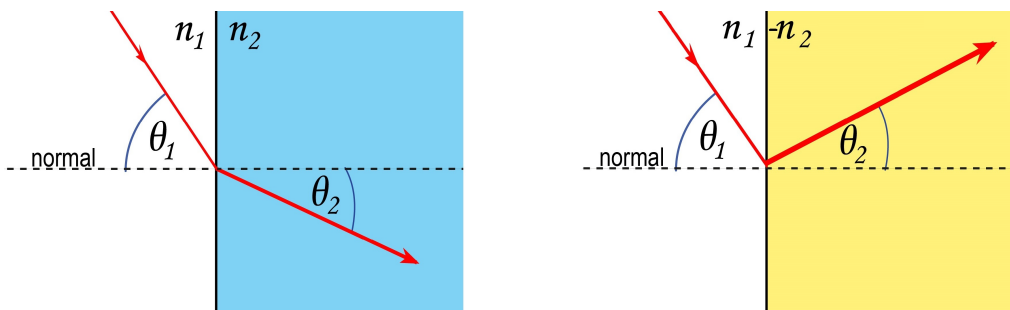


Figure 1.1: *Diagram comparing the path of a incident wave moving from a positive refractive index material (white) into another positive reactive index material (blue) or a negating refractive index metamaterial (yellow).*

## 1.2 Acoustic and Elastic Metamaterials

Manipulation of waves using materials with negative effective properties is not limited to electromagnetism, metamaterials have also been demonstrated in acoustics. The analogous properties to permittivity and permeability are bulk modulus (compressibility) and mass density. Liu (2000) created a material with negative effective elasticity which also broke the mass-density law by creating an 8x8x8 lattice of lead spheres encased in silicone rubber.

Jensen (2004) showed that to have a propagating plane wave inside of an acoustic medium, bulk modulus and mass density must have the same sign. This has the effect that the medium “expands upon compression (negative bulk modulus) and moves to the left when being pushed to the right (negative density) at the same time.” Jensen’s work focused on spheres in water, this was later criticised by Ding (2007) who asserted the single unit structure of the metamaterial was a flaw once all directions are considered. Ding instead advocated for the use of a double structure with one element having a strong monopole resonance while the other has a strong dipole resonance.

Liu (2011) gave the design for a remarkable device that was capable of producing both the monopole and dipole resonances in an easily demonstrated way. This chiral structure consists of a disk with two horizontal springs attached to its centre each connecting left and right disturbing bodies, these springs allow the disk to move left and right producing a dipole resonance. Additionally, two springs are attached at the circumference of the disk and to the disturbing bodies giving a rotational monopole resonance. Lia (2011) expanded Liu’s work to two dimensions by including a quadrupole resonance, allowing for sheer modulus control. This material presented different properties depending on the frequency of excitation: for high frequencies it could only transmit pressure waves (like a liquid), in lower frequency ranges it presents properties like an incompressible solid in some directions, but fluid-like in others.

Liu (2000 and 2005) showed that photonic crystals with a resonant structure could have negative effective mass density. Negative effective bulk modulus was later demonstrated using an array of Helmholtz resonators by Fang (2006). Ding (2007) theoretically combined these two works producing a material with simultaneously negative bulk modulus and mass density.

In 2009 Zhang successfully produced an acoustic lens with sub-wavelength elements ( $1/8$ th of the wavelength) capable of focusing ultrasonic sound waves in water. The lens was a matrix of Helmholtz resonators tuned to resonate at the ultrasonic frequency of interest. This acoustic lens achieved negative bulk modulus and mass density. Zhang notes that for higher quality focusing, the ratio of the refractive indices of the positive to negative materials should be  $-1$ . Pope (2011) also discusses the importance of matching some of the metamaterial’s properties to its surroundings. Matching of impedance is critical for applications such as cloaking because a large impedance change will cause scattering.

In most of the literature discussed here acoustic metamaterials, unlike electromagnetic meta-

materials, gain both of their negative properties from the same structure, rather than two separate structures in tandem; however, they both take advantage of resonances intrinsic to the medium in order to achieve this behaviour. One other common factor is the need for the structure of the metamaterial to be smaller than the wavelength of the propagating wave. It is important to note that these papers do not achieve negative mass or stiffness, indeed this is impossible. Instead these properties are emulated due to resonant behaviour, and cannot be achieved in the steady state.

### 1.3 Actively Controlled Metamaterials

Akl (2010) and Baz (2009 and 2010) produced an extensive theoretical analysis of acoustic active metamaterials with tunable density using piezoelectric elements. This work was combined in Akl and Baz (2013) where a one dimensional acoustic metamaterial was described where both bulk modulus and density were controllable. Like most of the previously referenced work, two separate structures are responsible for controlling the two parameters. While not directly applicable to this project as it does not deal with pushing density or bulk modulus negative, it does provide analysis of the methods of active control and their effects on bandwidth when used in fluids.

Popa (2013) experimentally demonstrated an acoustic active metamaterial that was able to achieve a range of densities, both positive and negative, while bulk modulus was kept almost constant. In a separate experiment they were able to tune bulk modulus over a range of positive values while keeping density constant. Interestingly Popa was able to demonstrate negative refraction with a positive refractive index (thereby not requiring simultaneously negative density and bulk modulus). This was achieved by methods discussed more fully in Pendry (2004 and 2008). To summarise, the transmission coefficients must be positive but without any complete phase wraps occurring.

In 2010 Pope suggested designs for actively controlled viscoelastic locally resonant metamaterials capable of producing double negative behaviour in a solid-state medium. One notable property of the suggested medium is the lack of need for a static connection point for the resonators, unlike Helmholtz resonators, while still able to produce the monopole and dipole resonances required for double negativity. Another notable finding from inspection of the equations of motion of the medium is that the control system induced resonance can be reduced by minimising mass and stiffness. Options for control of the medium are explored, such as the control perimeters being extended to adjacent unit cells. Additionally the possibility of adjustable stiffness or damping of the medium are mentioned. In a later paper (2012) Pope refined this design to include actuator dynamics and provide a basis for implementation. The work contains simulation on the two potential forms of actuation, namely reactive and inertial. Reactive actuators are shown to have a significant advantage in that their controllers can have gains orders of magnitude larger than inertial actuators and still maintain stability, they are also capable of larger bandwidth with the same model. Unfortunately reactive actuation is difficult if not impossible to realise in higher dimensions due to each unit cell requiring a fixed point to actuate against. This work constrains itself to

production of a one dimensional actively controlled system capable of producing a negative refractive index. It is noted that, though a one dimensional system is not of much practical use, it can be generalised to higher dimensions. Pope also notes the control force applied by an inertial actuator is limited by the inertial mass. This contrasts with the findings of Pope's 2010 paper, where mass and stiffness should be minimised. As such it may be that the inertial mass has an optimised value in terms of minimising actuator force requirement while maximising the force the actuator can produce. As discussed in Veselago (1967) a key test for this system is that waves should propagate through the medium with positive group velocity but negative wave velocity.

In Pope 2012 and 2014, physical test designs were realised. These tests were the first time a load-bearing material, with actively controllable parameters, produced simultaneously negative modulus and density. One of the advantages of this system is the tunability of the parameters, in this case the double negative band was achieved below 50Hz, lower than was achieved in earlier work. For this series of work, the control system is critical for emulation of cross coupling, as required to produce the simultaneous dipole and monopole resonance.

Pope (2011) explores the need for impedance matching in metamaterials. Impedance must match the surroundings to minimise reflection. Pope shows through simulation that it is theoretically possible to produce double negative behaviour while simultaneously perfectly matching impedance with a surrounding body across the whole frequency spectrum. However, he notes this would be extremely challenging to realise due to the complexity of the control scheme, especially considering inertial actuation. Impedance matching may not be necessary for seismic cloaking; however, for many other forms of cloaking it will be critical.

Pope clearly identified a hole in current literature; use of active control allows for deepening and widening of the resonant troughs in both effective mass and stiffness. It is possible to produce this negative mass and stiffness behaviour without control if components have low damping and are carefully selected; however, this results in limited bandwidth and frequency. This project seeks to build on the the work of Pope by miniaturising the actively controlled load-bearing metamaterial and by producing hardware capable of generalising the work to two dimensions.

## 1.4 Motivation

Apart from those mentioned in the literature, active vibration cloaking has several large predictable applications:

1. Cloaking of buildings from earthquakes and other disturbances: a building built on a vibration cloaking device would not be damaged by earthquakes as the vibrations would pass around the foundations without disturbing them.
2. Cloaking of submarines from SONAR (SOund Navigation And Ranging): a submarine or other seagoing vessel surrounded by a cloaking device would be invisible from SONAR detection as no waves would be reflected from the submarine, rather they would pass around.
3. Cloaking of vibration sensitive equipment in challenging environments.

Additionally as an emerging technology with technological readiness level of around three, it is likely that many other applications will be found as the technology develops.

This project seeks to address several limitations within the literature:

1. Limited and fixed bandwidth of the double negative region.
2. Large, heavy, designs requiring expensive actuation.
3. Active actuation in more than one dimension.

## 1.5 Initial Design

Figure 1.2 shows a possible implementation of the system in two dimensions. This design was received in a private communication with Dr Simon Pope and represents his initial vision for the project. It is included here for visualisation of a plausible design. The red disks are the inertial actuators, in this case, speaker coils. The blue cuboids are accelerometers. Each dovetail joint would have some spring ( $k_t$ ) and damping ( $c_t$ ) constants associated with it. The green and yellow objects are embedded computers able to implement control algorithms and communicate with their neighbours.

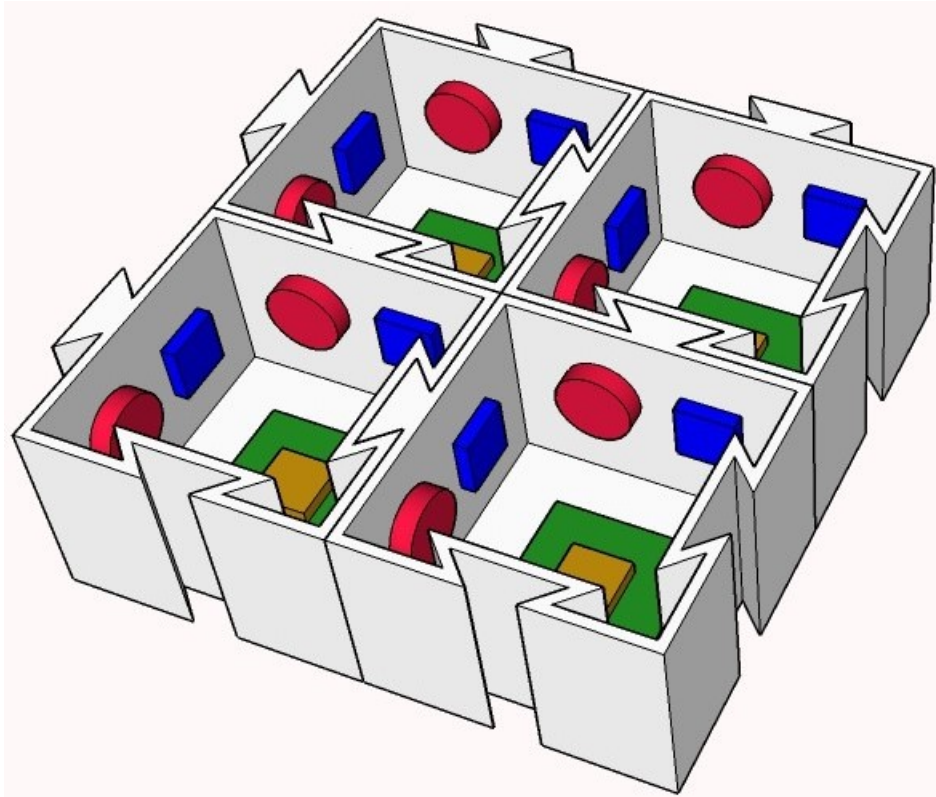


Figure 1.2: *Diagram showing an example of how the system may look in two dimensions.*

## 1.6 Project Aim and Objectives

### 1.6.1 Aim

Design, simulate, construct and test a unit cell with control, sensing and actuation sufficient to have both negative effective density and elasticity when part of a homogeneous pattern of unit cells. This unit cell should be capable of achieving this double negative behaviour in up to two dimensions, without the use of fixed points and reactive actuation, for input pressure or shear waves of  $> 0\text{Hz}$ .

### 1.6.2 Basic Objectives

- Conduct a literature review on passive and active mechanical metamaterials.
  - Sensing and actuation approaches and their effect on performance.
  - Topology of unit cell placement and shape.
- Investigate the characteristics required of each component to achieve double negative behaviour.
- Develop an easily repeatable design for the unit cells which is usable in both one and two dimensional arrays.

### 1.6.3 Advanced Objectives

- Design control algorithms capable of producing the double negative behaviour in one dimensional arrays.
- Simulate and analyse performance of an array of multiple cells in one dimension.
- Construct multiple unit cells.
- Test, analyse and validate the performance of an array of multiple cells in one dimension.

### 1.6.4 Objectives Beyond the State of the Art

- Design control algorithms capable of producing the double negative behaviour in two dimensions.
- Simulate and analyse the performance of this design for multiple cells in two dimensions.
- Test, analyse and validate the performance of an array of multiple cells in two dimensions.

## 1.7 Project Management

A Gantt chart indicating progress against the work program is included in Figure 5.1.

### 1.7.1 Resources

1. Dr Simon Pope.
2. Departmental technical staff.
3. University library and access to journal archives.
4. Existing hardware from previous larger scale experiments.
5. £200 in budget for hardware.
6. Laboratory access.
7. Powerful desktop computers in the Diamond building for running simulations.

### 1.7.2 Risks

1. Components arriving late.
2. Construction delays.
3. Time management of parallel work.
4. Delays in core activities resulting in subsequent tasks not being able to start, e.g. components cannot be ordered before simulation and specification has been completed.
5. Misunderstanding of theory resulting in carried forward errors.
6. Running out of budget.
7. Not having access to tools and machines outside of departmental open times.

### 1.7.3 Risk Management

1. Components will be ordered as early as possible and with fastest available shipping so that parts lost in transit can be identified and replaced as quickly as possible.
2. Construction delays will be mitigated through simple design of the components, thereby reducing the difficulty of manufacture.
3. A Gantt chart (Figure 5.1) has been produced to provide an outline of the time required for each project stage, this will be followed wherever possible.
4. Key areas such as modelling and simulation have been identified as high priority as several other stages are dependent on them, special care will be given to these sections to avoid mistakes being carried forward.
5. In addition to item 4, regular meetings to discuss work and progress with Dr Pope will reduce the risk of mistakes being carried forward.
6. Components will be carefully evaluated before buying large numbers, though this may be balanced against risk 4 (Delays in core activities).
7. Some tools may be purchased for use outside of departmental availability if sufficient budget is available.

# Chapter 2

## Modelling and Simulation

The objective of modelling the system is to follow, validate and expand on the previous work of Pope (2014). The model will be used for component selection and for controller design. A list of all used notation is given in Section 2.2.

The one dimensional system of cells will be modelled as part of an infinite chain of cells, though as will become apparent from the equations, each cell is only directly effected by the movements of adjacent cells. The resulting material will be a homogeneous vector of cells, meaning this model is easily adapted to any number of cells. Figure 2.1 shows the arrangement with the single cell being modelled highlighted in orange. The goal of the modelling and control design is to produce a system which emulates the behaviour that would be expected of the system in Figure 2.2 where both  $m$  and  $k$  are negative.

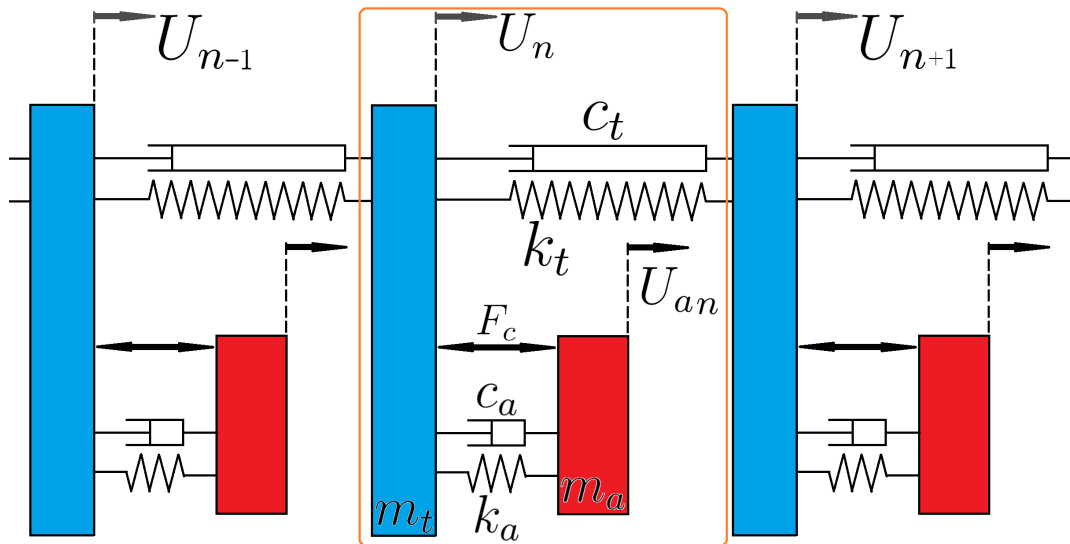


Figure 2.1: *Diagram of the system to be modelled.*

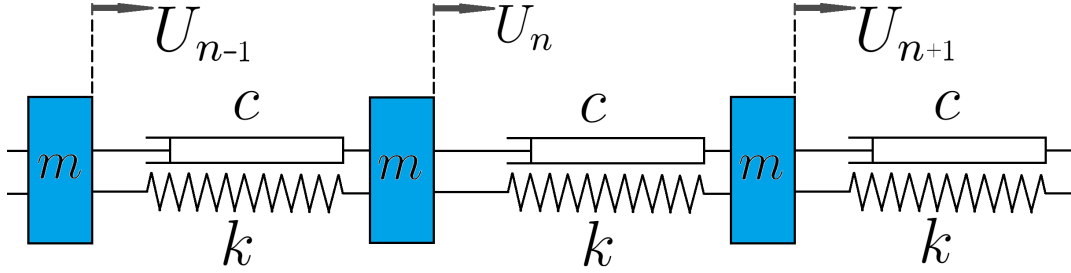


Figure 2.2: *Diagram of the system to be emulated using the actively controlled system.*

## 2.1 Modelling Simplifications

- Rotation of the masses is neglected for this model as in the real system rotation will either be negligible or the masses will be prevented from rotating through symmetrical force placement or other methods such as rail mounting. In this way the model is confined to one dimension with two degrees of freedom ( $U_n$  and  $U_{an}$ ).
- Actuator dynamics responsible for producing the control force  $F_c$  are ignored in the initial modelling.
- Air resistance is negligible, though a very simple first order approximation may be introduced by increasing the modelled damping values  $c_t$  and  $c_a$ .
- All other resistances to motion and damping effects are assumed to be effectively modelled through modification of the  $c_t$  and  $c_a$  terms.
- The modelled springs and dampers are assumed to have constant rates that are time and frequency invariant.
- The coil gains  $g_c$  and  $g_{bEMF}$  are constant.
- Resistance ( $r$ ) and inductance ( $l$ ) of the actuator coil are linear time invariant. This assumption may become invalid should the actuators be run for long periods of time or at higher currents, this would result in changing inductance and resistance due to heating of the actuator coil.

## 2.2 Notation

Capital letters for variable names denote time variance.

### Displacement

$U_n$	Displacement of transmission mass from rest position ( $m$ ).
$U_{n-1}$	Displacement of the left adjacent transmission from rest position ( $m$ ).
$U_{n+1}$	Displacement of the right adjacent transmission from rest position ( $m$ ).
$U_{an}$	Displacement of inertial resonant actuation mass from rest position ( $m$ ).

### Mass

$m_t$	Mass of the transmission mass ( $Kg$ ).
$m_a$	Mass of the resonant actuation mass ( $Kg$ ).
$m_{ep}$	Effective mass of the passive system ( $Kg$ ).
$m_e$	Effective mass of the active system ( $Kg$ ).

### Stiffness & Damping

$k_t$	Spring rate of the transmission mass spring ( $N/m$ ).
$k_a$	Spring rate of the resonant actuation mass spring ( $N/m$ ).
$k_{ep}$	Effective stiffness of the passive system ( $N/m$ ).
$k_e$	Effective stiffness of the active system ( $N/m$ ).
$c_t$	Damping rate of the transmission mass damper ( $N/ms^{-1}$ ).
$c_a$	Damping rate of the of the resonant actuation mass damper( $N/ms^{-1}$ ).

### Control Gains

$g_m$	Gain on the mass control term.
$g_k$	Gain on the stiffness control term.

### Force

$F_c$	Force from the actuator ( $N$ ).
$F_m$	Force required negative mass ( $N$ ).
$F_k$	Force required negative stiffness ( $N$ ).

### Actuator Dynamics

$g_c$	Gain of the actuator coil.
$I$	Current in the actuator coil ( $A$ ).
$V$	Voltage across the actuator coil ( $V$ ).
$V_{bEMF}$	Back EMF across the coil the actuator coil ( $V$ ).
$g_{bEMF}$	Back EMF gain across the coil the actuator coil.
$r$	Resistance of the actuator coil ( $R$ ).
$l$	Inductance of the actuator coil ( $H$ ).

### Miscellaneous

$\omega$	Angular frequency ( $rads/s$ ).
$s = \omega i$	Laplace variable.

## 2.3 Passive Transmission and Actuator Mass System

### 2.3.1 Modelling

The control force  $F_c$  will be left in for greater continuity between the passive and active system, though, clearly for the true passive system  $F_c = 0$ . First the equation of motion of the transmission mass must be derived, this is done using  $F = ma$ ; by equating all of the forces acting on  $m_t$  to the mass acceleration of  $m_t$ . The result is then converted to the frequency domain using the Laplace transform and simplified to Equation 2.1.

$$\begin{aligned} \ddot{U}_n m_t &= k_a(U_{an} - U_n) + c_a(\dot{U}_{an} - \dot{U}_n) + k_t(U_{n-1} - 2U_n + U_{n+1}) + c_t(\dot{U}_{n-1} - 2\dot{U}_n + \dot{U}_{n+1}) - F_n \\ U_n m_t s^2 &= k_a(U_{an} - U_n) + c_a(U_{an}s - U_n s) + k_t(U_{n-1} - 2U_n + U_{n+1}) + c_t(U_{n-1}s - 2U_n s + U_{n+1}s) - F_n \\ U_n m_t s^2 &= (k_a + c_a s)(U_{an} - U_n) - F_n + (k_t + c_t s)(U_{n-1} - 2U_n + U_{n+1}) \end{aligned} \quad (2.1)$$

Next the equation of motion of the resonant mass must be derived as in Equation 2.2. This equation is then rearranged and simplified resulting in Equation 2.3

$$F_n - k_a (U_{an} - U_n) - c_a (U_{an} s - U_n s) = U_{an} m_a s^2 \quad (2.2)$$

$$U_{an} = \frac{F_n + U_n(k_a + c_a s)}{m_a s^2 + c_a s + k_a}$$

Now let

$$B_a = k_a + c_a s \quad \& \quad B_t = k_t + c_t s$$

Such that

$$U_{an} = \frac{F_n + B_a U_n}{m_a s^2 + B_a} \quad (2.3)$$

By substitution of the resonant mass equation into the transmission mass equation and through simple operations we arrive at the dynamics of the passive system Equation 2.4).

$$\begin{aligned} B_a \left( \frac{F_n + B_a U_n}{m_a s^2 + B_a} - U_n \right) - F_n + B_t (U_{n-1} - 2U_n + U_{n+1}) &= U_n m_t s^2 \\ B_a \left( \frac{F_c - U_n m_a s^2 + B_a U_n - U_n B_a}{m_a s^2 + B_a} \right) - F_c + B_t (U_{n-1} - 2U_n + (U_{n+1})) &= U_n m_t s^2 \\ \frac{B_a F_c - B_a U_n m_a s^2}{m_a s^2 + B_a} - F_c + B_t (U_{n-1} - 2U_n + (U_{n+1})) &= U_n m_t s^2 \\ \frac{B_a F_c}{m_a s^2 + B_a} - F_c + B_t (U_{n-1} - 2U_n + (U_{n+1})) &= U_n s^2 \left( m_t + \frac{B_a m_a}{m_a s^2 + B_a} \right) \\ \frac{F_c B_a}{m_a s^2 + B_a} - \frac{F_c (m_a s^2 + B_a)}{m_a s^2 + B_a} + B_t (U_{n-1} - 2U_n + (U_{n+1})) &= U_n s^2 \left( m_t + \frac{B_a m_a}{m_a s^2 + B_a} \right) \end{aligned}$$

$$\begin{aligned}
F_c \left( \frac{B_a}{m_a s^2 + B_a} - \frac{m_a s^2 + B_a}{m_a s^2 + B_a} \right) + B_t(U_{n-1} - 2U_n + (U_{n+1})) &= U_n s^2 \left( m_t + \frac{B_a m_a}{m_a s^2 + B_a} \right) \\
F_c \left( \frac{B_a - m_a s^2 - B_a}{m_a s^2 + B_a} \right) + B_t(U_{n-1} - 2U_n + (U_{n+1})) &= U_n s^2 \left( m_t + \frac{B_a m_a}{m_a s^2 + B_a} \right) \\
\frac{-F_c m_a s^2}{m_a s^2 + B_a} + B_t(U_{n-1} - 2U_n + (U_{n+1})) &= U_n s^2 \left( m_t + \frac{B_a m_a}{m_a s^2 + B_a} \right) \quad (2.4)
\end{aligned}$$

Equation 2.5 describes the effective mass of the passive system ( $m_{ep}$ ), clearly for this to be negative  $\frac{B_a m_a}{m_a s^2 + B_a}$  must be negative and have magnitude larger than  $m_{ep}$ .

When the system is passive  $F_c = 0$  and  $k_{ep} = B_t$  as given in Equation 2.6.

$$m_{ep} = m_t + \frac{B_a m_a}{m_a s^2 + B_a} = m_t + \frac{c_a s m_a + k_a m_a}{m_a s^2 + c_a s + k_a} = m_t + \frac{c_a m_a \omega i + k_a m_a}{-m_a \omega^2 + c_a \omega i + k_a} \quad (2.5)$$

$$k_{ep} = B_t = k_t + c_t s = k_t + c_t \omega i \quad (2.6)$$

### 2.3.2 Simulation

Plotting the response of  $m_{ep}$  and  $k_{ep}$  across the frequency spectrum (Figure 2.3) illuminates the systems behaviour. The values used for the simulation are largely arbitrary and were selected to best demonstrate the behaviour of interest and for normalised resonant frequencies, they are not representative of the true system's values and will be repeated later as the hardware design is developed. This simulation was done using the code given in Appendix 6.1.

The  $m_{ep}$  plot shows two resonant peaks: one positive (at  $0.9 \text{ rads/s}$ ) and one negative (at  $1.1 \text{ rad/s}$ ). The frequency between these peaks is where the phase of the resonant mass flips by  $180^\circ$ . These peaks are caused by the denominator of the frequency variable component ( $-m_a \omega^2 + c_a \omega i + k_a$ ) crossing over zero resulting in the fraction becoming very large. It can be seen in the  $k_{ep}$  plot that, due to the only real component of  $k_{ep}$  being  $k_t$ , which is constant, the response is flat. The value of  $c_a$  was selected to be comparatively small as damping acts to suppress the resonant behaviour of the cell. As discussed in the literature by Pope (2014) the imaginary components, for example the  $c_t \omega i$  term, represent the transmission losses. This would seem logical given its attachment to the damping coefficients.

The objective of active control is to deepen the resonant trough in  $m_{ep}$  and create a resonant trough in  $k_{ep}$  so as to force negativity. Another objective is to broaden the trough, thereby increasing the bandwidth of the negativity. It is possible to produce this negative mass behaviour in a passive system with carefully selected components and low damping; however, this presents issues as discussed in the literature, namely limited bandwidth and frequency. Active control, when added to a passive system, allows for broader bandwidth of negativity.

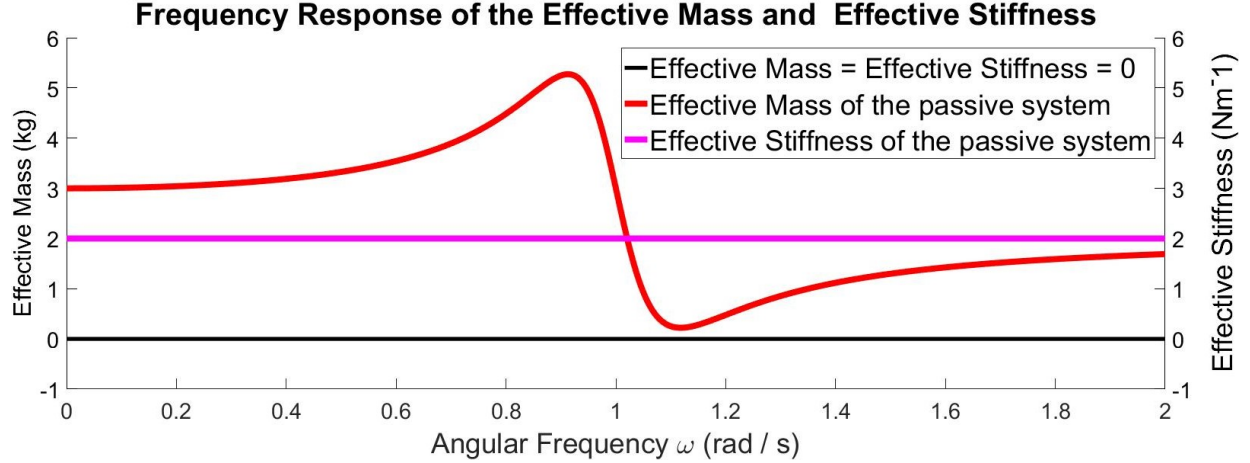


Figure 2.3: Graph showing the real component of the frequency response of the effective mass ( $m_{ep}$ ) and effective stiffness ( $k_{ep}$ ) of the passive system with simulation values of  $m_t = 2\text{kg}$ ,  $m_a = 1\text{kg}$ ,  $c_a = 0.2\text{Nsm}^{-1}$ ,  $k_a = 1\text{Nm}^{-1}$ ,  $c_t = 2\text{Nsm}^{-1}$  and  $k_t = 2\text{Nm}^{-1}$

## 2.4 Control Forces

A control force ( $F_c$ ) can act between the transmission and resonant mass with the objective of achieving double negativity. This control force should consist of the sum of the forces required to control the effective mass ( $F_m$ ) and the effective stiffness ( $F_k$ ) as in equation 2.7.

$$F_c = F_k + F_m \quad (2.7)$$

In order for the effective mass to be negative an external force ( $F_{ex}$ ) acting on the cell should result in an acceleration opposite to that normally observed,  $F_{ex} = -m\ddot{U}_n$ . From the system diagram, the positive control force ( $F_c$ ) acts in the opposite direction to the displacement ( $U_n$ ) cancelling this negative. This results in a control force ( $F_m$ ) as in Equation 2.8, where  $g_m$  is the control gain for the effective mass. This increases the dipole resonance of the system.

$$F_m = g_m U_n s^2 \quad (2.8)$$

In order for the effective stiffness to be negative an external force ( $F_{ex}$ ) acting on the cell should result in an extension opposite to that normally observed,  $F_{ex} = -kx$ , where  $x$  is the displacement from the rest position in the direction of the external force ( $F_{ex}$ ). This results in a control force, ( $F_k$ ) as in Equation 2.9, where  $g_k$  is the control gain for the effective stiffness. The inclusion of the displacements of adjacent cells within the control law of the cell introduces the cross coupling and monopole resonance required for negative effective stiffness. The total force needed ( $F_c$ ) is given by Equation 2.10.

$$F_k = g_k(U_{n-1} - 2U_n + U_{n+1}) \quad (2.9)$$

$$F_c = g_m U_n s^2 + g_k(U_{n-1} - 2U_n + U_{n+1}) \quad (2.10)$$

## 2.5 Actively Controlled System

### 2.5.1 Modelling

By including the control laws from the previous section, the equations of the unit cell can be augmented.

Substitution of  $F_c$  (Equation 2.10) into the passive system (Equation 2.4), followed by substitution of the passive mass ( $m_{ep}$ , Equation 2.5) results in Equation 2.11. Equations 2.12 and 2.13 give the effective mass ( $m_e$ ) and effective stiffness ( $k_e$ ) for the actively controlled system.

$$\begin{aligned}
& \frac{-(g_m U_n s^2 + g_k (U_{n-1} - 2U_n + U_{n+1})) m_a s^2}{m_a s^2 + B_a} + B_t (U_{n-1} - 2U_n + (U_{n+1})) = U_n s^2 m_{ep} \\
& B_t (U_{n-1} - 2U_n + (U_{n+1})) - \frac{m_a s^2 g_k (U_{n-1} - 2U_n + U_{n+1})}{m_a s^2 + B_a} = U_n s^2 m_{ep} + \frac{m_a s^2 g_m U_n s^2}{m_a s^2 + B_a} \\
& (U_{n-1} - 2U_n + U_{n+1}) \left( B_t - \frac{m_a s^2 g_k}{m_a s^2 + B_a} \right) = U_n s^2 m_{ep} + \frac{m_a s^2 g_m U_n s^2}{m_a s^2 + B_a} \\
& (U_{n-1} - 2U_n + U_{n+1}) \left( B_t - \frac{m_a s^2 g_k}{m_a s^2 + B_a} \right) = U_n s^2 \left( m_t + \frac{B_a m_a}{m_a s^2 + B_a} \right) + \frac{m_a s^2 g_m U_n s^2}{m_a s^2 + B_a} \\
& (U_{n-1} - 2U_n + U_{n+1}) \left( B_t - \frac{m_a s^2 g_k}{m_a s^2 + B_a} \right) = U_n s^2 \left( m_t + \frac{B_a m_a + m_a s^2 g_m}{m_a s^2 + B_a} \right) \\
& (U_{n-1} - 2U_n + U_{n+1}) \left( B_t - \frac{m_a s^2 g_k}{m_a s^2 + B_a} \right) = U_n s^2 \left( m_t + m_a \frac{s^2 g_m + B_a}{m_a s^2 + B_a} \right) \quad (2.11)
\end{aligned}$$

$$m_e = m_t + m_a \frac{g_m s^2 + B_a}{m_a s^2 + B_a} = m_t + m_a \frac{g_m s^2 + c_a s + k_a}{m_a s^2 + c_a s + k_a} = m_t + m_a \frac{-g_m \omega^2 + c_a \omega i + k_a}{-m_a \omega^2 + c_a \omega i + k_a} \quad (2.12)$$

$$k_e = B_t - \frac{m_a s^2 g_k}{m_a s^2 + B_a} = c_t s + k_t - \frac{m_a s^2 g_k}{m_a s^2 + c_a s + k_a} = c_t \omega i + k_t - \frac{-m_a g_k \omega^2}{-m_a \omega^2 + c_a \omega i + k_a} \quad (2.13)$$

The effective stiffness has been augmented to have a real component which is frequency dependent. The denominator  $-m_a \omega^2 + c_a \omega i + k_a$  will initially be positive for low frequencies; however, with increasing  $\omega$  its value will pass through zero towards negative infinity. Passing through zero will cause a large resonant spike at the same frequency as the phase swaps by  $180^\circ$  giving the response the desired shape.

By increasing the control gains for the effective mass ( $g_m$ ) and effective stiffness ( $g_k$ ) the amplitude of the resonant peaks can be manipulated to push the effective mass and effective stiffness negative.

## 2.5.2 Actuator Dynamics

The actuator dynamics will now be modelled. A diagram of the voice coil is included in Figure 2.4.

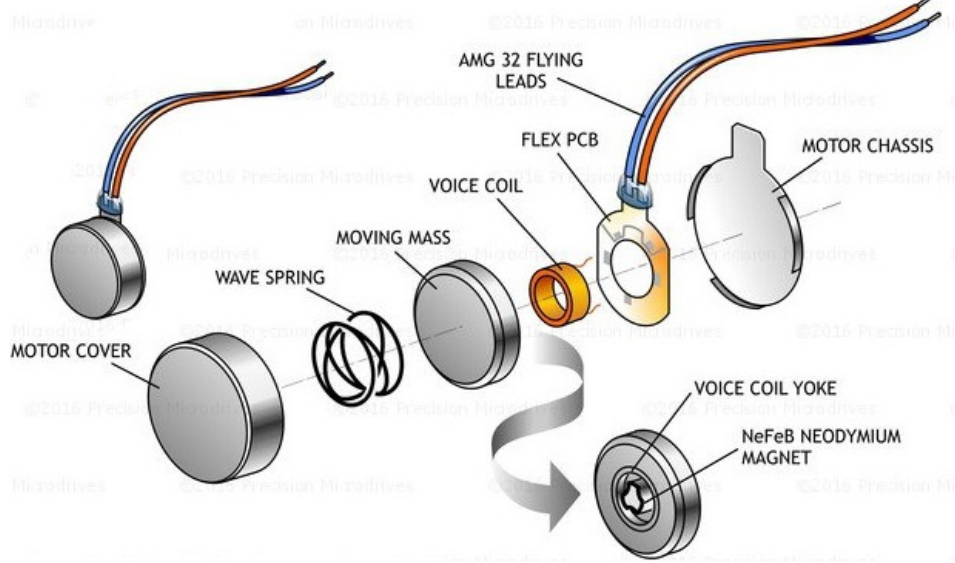


Figure 2.4: Diagram showing the construction of the Precision Microdrives linear resonant actuator. Taken from Precision Microdrives promotional material. (2014)

Equation 2.14 describes the force produced by the voice coil for a current  $I$  where  $g_c$  is a gain associated with the coil. Equation 2.15 contains Kirchoff's law, the inductance current voltage relationship, and the back EMF produced by the cone moving through the inductor's magnetic field where  $g_{bEMF}$  is the counter-electromotive force gain for the coil. Equation 2.16 describes the total voltage across the coil.

$$F_c = g_c I \quad (2.14)$$

$$V = Ir \quad V = l\dot{I} \quad V = g_{bEMF}\dot{x} \quad (2.15)$$

$$V = Ir + l\dot{I} + V_{bEMF} \quad (2.16)$$

By substitution the relationship between input voltage across the actuator and output force is found, as in Equation 2.17. If this equation is substituted into the control law model (Equation 2.10) and following the derivation as before, a more accurate approximation to the real systems behaviour will be found. Equation 2.17 also allows for the control voltage applied by the controller to the actuators to be more precisely adjusted based on the state of the system such that the actual control forces more closely resemble the desired values.

$$F_c = -g_c \frac{V - g_{bEMF}(U_{ans} - U_n s)}{r + ls} \quad (2.17)$$

### 2.5.3 Simulation

Figure 2.5 show the simulated frequency response of the real components of the effective mass and effective stiffness ( $m_e$  and  $k_e$ ). The same values were used as in the passive system simulation (Figure 2.3) for the reasons explained previously.

By incorporating active control into the system, simultaneous negativity of both  $m_e$  and  $k_e$  are achieved. The resonant peaks of  $m_e$  have increased in magnitude over  $m_{ep}$ . The flat  $k_{ep}$  curve has been manipulated to having similar resonant behaviour to  $m_{ep}$ . The objectives of the simulation have been achieved. The model can now be used to identify suitable components for the hardware and stability analysis can be conducted to find ideal control gains.

As with the passive system, the peaks are caused by the denominator of the frequency variable component ( $-m_a\omega^2 + c_a\omega i + k_a$ ) crossing over zero resulting in the fraction becoming very large. This occurs where the phase of the resonant mass flips by  $180^\circ$  at  $1 \text{ rad/s}$ .

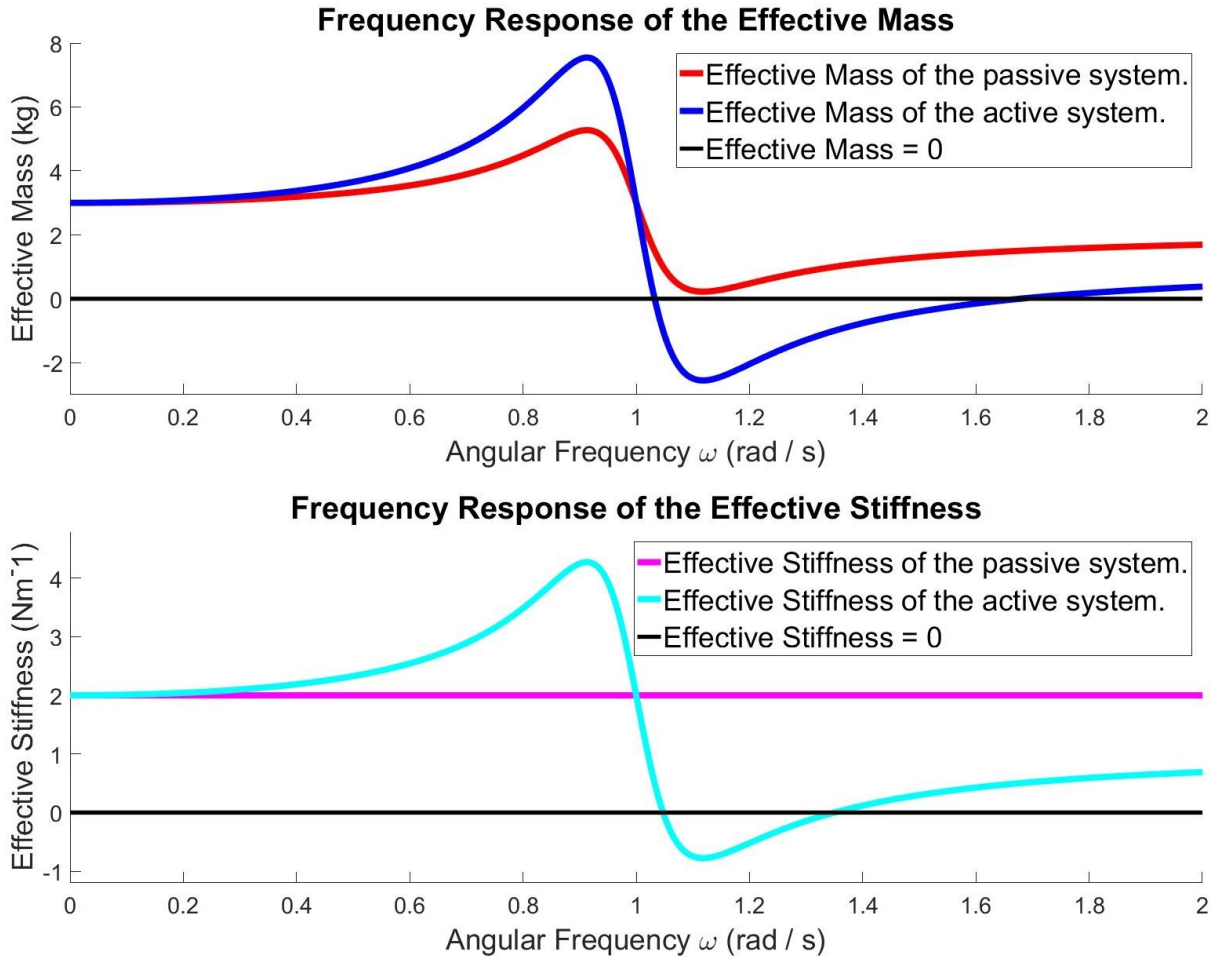


Figure 2.5: Graphs showing the real components of the frequency response of the effective mass ( $m_e$ ) and effective stiffness ( $k_e$ ) of the system.  $m_t = 2\text{kg}$ ,  $m_a = 1\text{kg}$ ,  $c_a = 0.2\text{Nsm}^{-1}$ ,  $k_a = 1\text{Nm}^{-1}$ ,  $c_t = 2\text{Nsm}^{-1}$ ,  $k_t = 2\text{Nm}^{-1}$ . The control gains were  $g_m = -1$  and  $g_k = -1$ .

# Chapter 3

## Hardware Design

### 3.1 Design Objectives

In order to improve the performance of the system the actuation mass should be as large as possible compared to the rest of the system mass. Since the actuation mass cannot be modified, it follows that the rest of the system should be as light as possible. The cells should be stiff and allow for good force transfer. The design should be easily modified and manufactured at low cost as this is a piece of research hardware and will be continually adapted and updated. The design should be constructed from modular elements, easily assembled into the desired configuration allowing for both 1D and 2D layouts.

### 3.2 Cell Topology

Initially several shapes for the cells were considered. Perfect tessellation is desirable to allow for the greatest force transfer between cells, while rigidity is also desirable to maintain the lumped spring assumption from the modelling. A circle would allow for the greatest internal area per unit circumference, this would allow the least material to be used for the cell walls but would not be tessellated on the 2D plane perfectly. Hexagons are often found in nature due to being the closest approximation to a circle which can be perfectly tessellated, this was proved by Thomas Hales (2001). The approximation to a circle allows for side faces to have the shortest length possible which reduces flex.

While hexagonal prisms can be tessellated uniformly in two dimensions, this cannot be done uniformly in x, y, and z directions. While this is not a disadvantage within the scope of this project, the eventual goal of the field of research will be a two dimensional structure, as such this should be considered. The use of a hexagon does not decouple the x and y directional actuator forces making analysis and control more complex. In order for good force transfer in two dimensions the shape should be a space-filling polyhedron, that is a polyhedron which can tessellate euclidean space in 3D space using translations only. Only five space-filling polyhedra exist for 3D space, these are cube, hexagonal prism, rhombic dodecahedron, elongated dodecahedron, and truncated octahedron (Deza 2000). Of these only the cube is able

to decouple forces acting directly in the x, y and z directions. For this reasons the cube was selected as the basic shape of the cell.

### 3.3 Input/Output and Control

Input/Output (I/O) was achieved using the National Instruments (NI) ecosystem of products centred around LabVIEW system design software. NI-cDAQ-9178 CompactDAQ Chassis along with NI-9201 Voltage Input Modules and NI-9263 Voltage Output Modules were used. The NI-9201 is capable of measuring eight independent voltage channels within the range of  $\pm 10V$  with 12-Bit resolution and  $\pm 0.014V$  accuracy at 500kS/s(kHz). The NI-9263 is capable of outputting four independent voltage channels within the range of  $\pm 10V$ ,  $\pm 1mA$  with an accuracy of 0.02V at 100kS/s.

The actuator selected is best used at 175Hz giving a Nyquist sampling frequency of 350Hz, this is the theoretical minimum frequency the system should be sampled at to avoid information loss and aliasing. Practically 1750Hz would be a more acceptable sampling frequency. Both the NI-9263 and the NI-9201 have performance far beyond what is required for this use and cost £395 per unit and £1230 for the chassis; however, the units were available for use during the project.

### 3.4 Actuation

#### 3.4.1 Actuation

The Precision Microdrives C10-100 linear resonant actuator (LRA) has a resonant frequency of 175Hz. This is where the actuator is able to produce the greatest force, the rest of the hardware is therefore designed to operate around this frequency. The LRA is driven by an alternating current sine wave at the desired frequency, amplitude, and phase. This input signal is the only control parameter for the cell and ideally all three should be controllable during operation. The same drive will be used to provide the disturbing force to the cell array.

The LRAs require an input of 2V RMS and typical operating current of 69mA in order to deliver their rated force. The selected NI-9263 output device is not able to provide this current, a buffer circuit is therefore required. The Linear Technology LT1010 operational amplifier was selected for this purpose. At the time of selection LT1010s were the lowest cost amplifier which is was easily available and are also able to supply 150mA allowing for two LRAs to be powered with the same signal.

#### 3.4.2 Circuit Design

A circuit was designed for the LT1010 buffer amplifier on stripboard and was laid out such that several could be lined up allowing for amplification of many independent drive signals

for LRAs, this design consideration will allow the same basic circuit design to be scaled up as necessary as more cells are added for two and three dimensions.

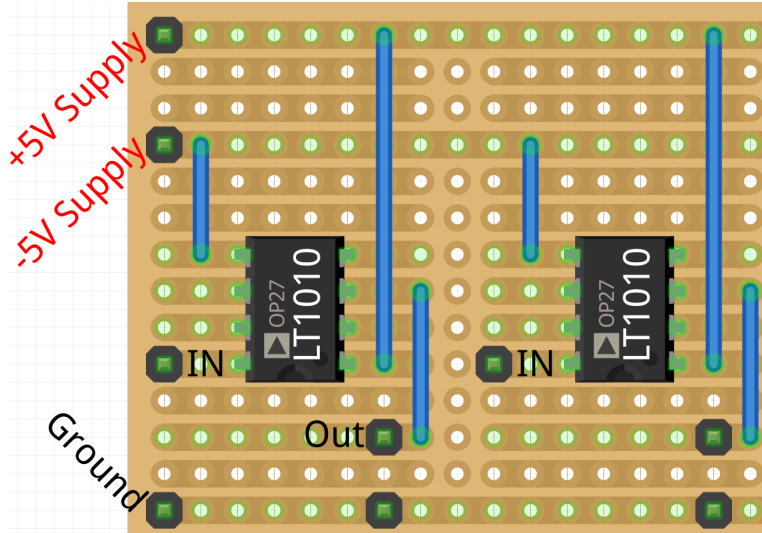


Figure 3.1: Diagram showing the stripboard design for two LT1010 buffer amplifiers used to power the LRAs.

## 3.5 Sensing

### 3.5.1 Acceleration

Each cell must be able to sense its own acceleration, velocity and displacement relative to the cells around it. The accelerometer used must have a bandwidth sufficient to capture all of the behaviour of the system. The actuators have a resonant frequency of 175Hz, it follows that the accelerometer must be able to capture all of the dynamics around that frequency.

The Analog Devices ADXL327 analogue accelerometer has a bandwidth which can be adjusted by altering the capacitance of surface mount capacitors, these capacitors act as low pass filters on the output. Equation 3.1 gives the relationship between capacitance ( $C_{(xyz)}$ ) and the bandwidth ( $f_{-3dB}$ ) of the filtering. The ADXL327 initially comes with a  $0.1\mu\text{F}$  capacitor filtering each output which gives a bandwidth of 50Hz, too low for the resonant frequency of the actuators. The capacitors are therefore removed and filtering is done within the control software.

$$f_{-3dB} = \frac{1}{2\pi(32k\Omega) * C_{(xyz)}} \approx \frac{5\mu\text{F}}{C_{(xyz)}} \quad (3.1)$$

The accelerometer contains a polysilicon surface held by springs above a silicon wafer, both the surface and the wafer act as plates of a capacitor. The capacitor plates are driven with two square waves in antiphase, the displacement of this surface unbalances the capacitor which is measured through observation of change in capacitance between the two plates.

### 3.5.2 Disturbing LRA Force

The force caused by the interaction of the cell with the disturbing LRA must be measured in order to extract the data required for performance analysis. A load cell was selected to measure the force from the disturbing actuator acting on the first cell. The disturbing force can act to both push and pull the first cell, the load cell must therefore be bi-directional, that is - measure both tensile and compressive forces. Initially S Beam load cells were explored as they directly measure tension and compression axially through the cell rather than shear forces such as with a beam load cell. Options such as the Futek LSB200 Miniature S Beam Load Cell were explored; however, the cost was found to be prohibitively expensive when ordering small numbers of units.

The Phidgets RB-Phi-203 100g Micro Load Cell (Figure 3.2) is a small double bending beam load cell capable of measuring force changes to a repeatability of  $\pm 50\text{mg}$  while also being low cost (£7 per unit). The RB-Phi-203 uses a pair of strain gauges designed to measure deformation in opposite directions. These strain gauges change resistance as they are deformed, the force required to deform the load cell beam is known so the force causing deformation can be easily found by measuring the change in resistance of the strain gauge. The resistance is measured using a Wheatstone bridge in the half bridge configuration. This device has a maximum output of  $600\mu\text{V}$  so will require amplification to be read.

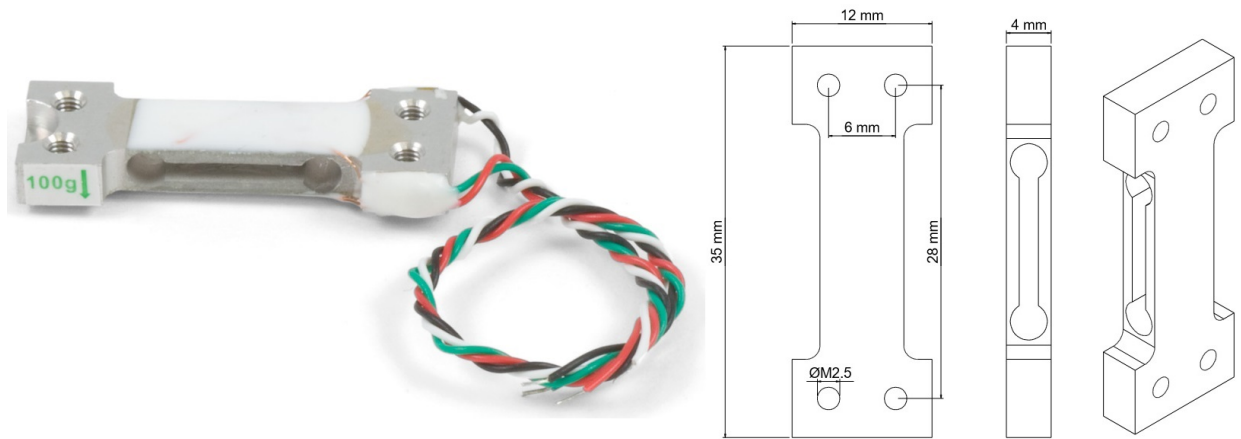


Figure 3.2: *Picture of the Phidgets RB-Phi-203 100g Micro Load Cell. Modified from Phidgets promotional material and data sheet (2013).*

### 3.5.3 Circuit Design

These small analog devices produce very small output currents requiring an instrumentation amplifier such that the outputs can be read without altering the voltage significantly. The Analog Devices AD623 is a very low cost instrumentation amplifier with an adjustable gain and a very high input impedance of  $2\text{G}\Omega$  resulting in very little current being drawn from the input device. This allows signals to be read while having a negligible affect on the signal

itself; without the use of a high input impedance amplifier reading the signals would cause distortion due to the current draw pulling the signal to ground. Figure 3.3 (right) shows a simplified operational amplifier representation of this device.

The typical input voltage of the AD623 is 5V; however, both positive and negative forces must be measured, therefore the readings must be biased to prevent readings below ground being lost. For this reason a bias of 2.5v is added, this is achieved using a potential divider between the +5v and ground rails. This will give a reasonably accurate offset, provided only a small current is drawn from the divider rail.

The AD623 has an adjustable gain which is programmed by the impedance appearing between Pin 1 and Pin 8. Equation 3.2 describes the relationship between the gain setting resistor ( $R_G$ ) and gain ( $G$ ). The rated output of the Phidgets RB-Phi-203 load cell is  $600\mu\text{V}$  for forces in each of the two directions. This output must be amplified to fill a larger proportion of the output range of 2.5V. Initially a gain of  $\frac{2.5\text{V}}{600 \times 10^{-6}} = 417$  may seem ideal as the output from the RB-Phi-203 would cover the entire range between 0V and 5V; however, on closer inspection of the data sheet it is clear that higher gains produce greater non-linearity in the range of interest (100-2000Hz). A lower gain of 210 was selected giving a desired gain setting resistance of  $470\Omega$ . With this gain the output from the load cell will be amplified to cover 1.26V of the available 2.5V range.

$$R_G = \frac{100k\Omega}{G - 1} \quad (3.2)$$

A circuit was designed for stripboard and was laid out in the same way as the LT1010 circuitry allowing several to be lined up for amplification of many signals from the various sensors. Figure 3.3 (left) shows two such circuits laid out on the same piece of stripboard.

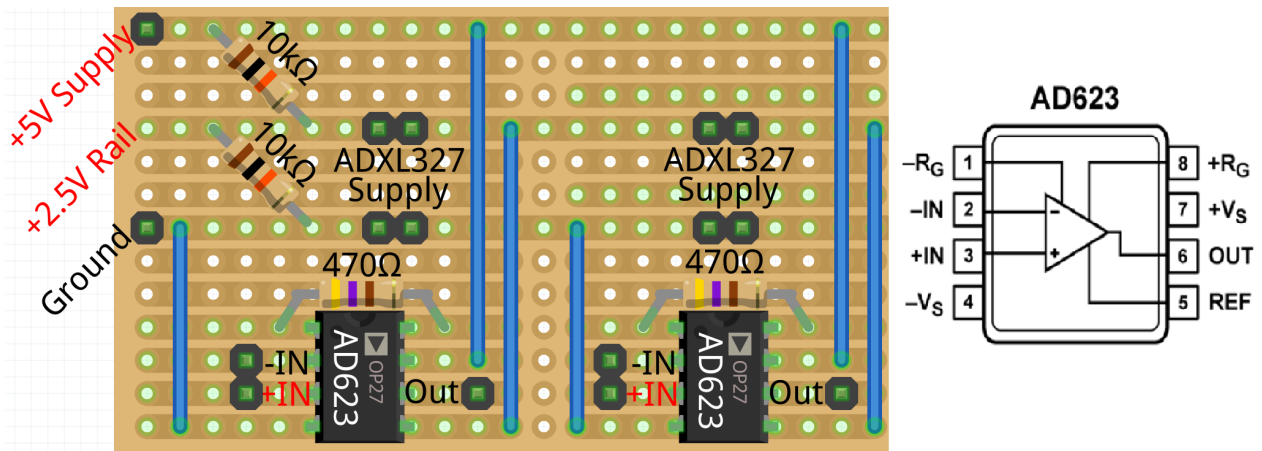


Figure 3.3: **Left:** Stripboard design for two AD623 amplifiers used to amplify the signals from the load cells and accelerometers. **Right:** Operational amplifier diagram of the AD623 taken from the datasheet (2012).

## 3.6 Transmission Mass Body

### 3.6.1 Material

A material selection package, Granta CES, was used to compare materials for the transmission mass body. CES contains a database of thousands of materials and their properties which can be plotted to identify promising options.

The body of the cell should be lightweight (low density) and stiff (high Young's modulus) while also being easy to manufacture and reasonably cheap. CES was used to plot Young's modulus / density on the y-axis and price per kilogram on the x-axis (Figure 3.4 (top)). Carbon fibre composites are excellent in terms of Young's modulus / density; however, they are expensive and difficult to manufacture; they require a mould for every unique part and layering of the fibres in resin. The search space is further limited to only include materials which are easy to manufacture, that is plastics excluding those containing fibres or particulates. Additionally results were filtered to only include those which can be formed through injection moulding, extruding or thermoforming.

From Figure 3.4 it is clear that the best choices are styrene (SMMA), polylactic acid (PLA) and polystyrene (PS). Styrene and polystyrene are very low density plastics resulting in an excellent Young's modulus to density ratio; however, they are brittle and more challenging to produce by additive manufacture (3D printing) which increases the difficulty of rapid prototyping. Polystyrene is also dissolved by many common solvents significantly limiting glues that can be used with it. Polylactic acid is an excellent material for additive manufacture allowing prototypes to be produced within hours of design, and for this reason was selected for the development stage of the hardware.

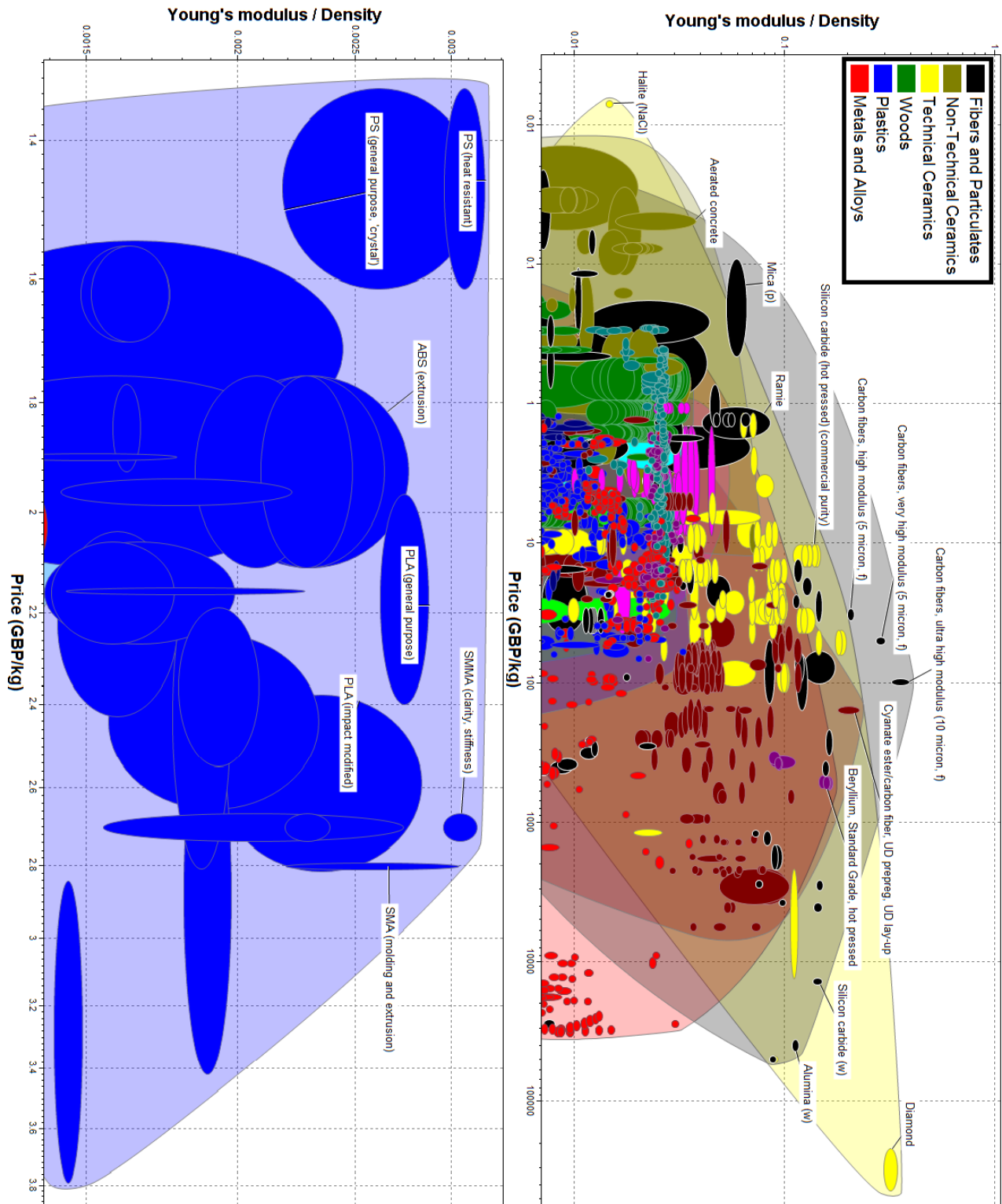


Figure 3.4: Graphs showing the properties of materials considered for the transmission mass body. **Top:** Unfiltered graph of all material groups available in CES. **Bottom:** Filtered graph of plastics.

### 3.6.2 Form

The cell was designed in the SolidWorks CAD program and then printed on a MakerBot Replicator 3D printer. Figure 3.5 shows the first design for the cell including two spring elements. The internal chamfered edge was designed to improve the rigidity of the corners while the indents on the internal faces were designed to hold the LRAs in place and allow for consistent placement.

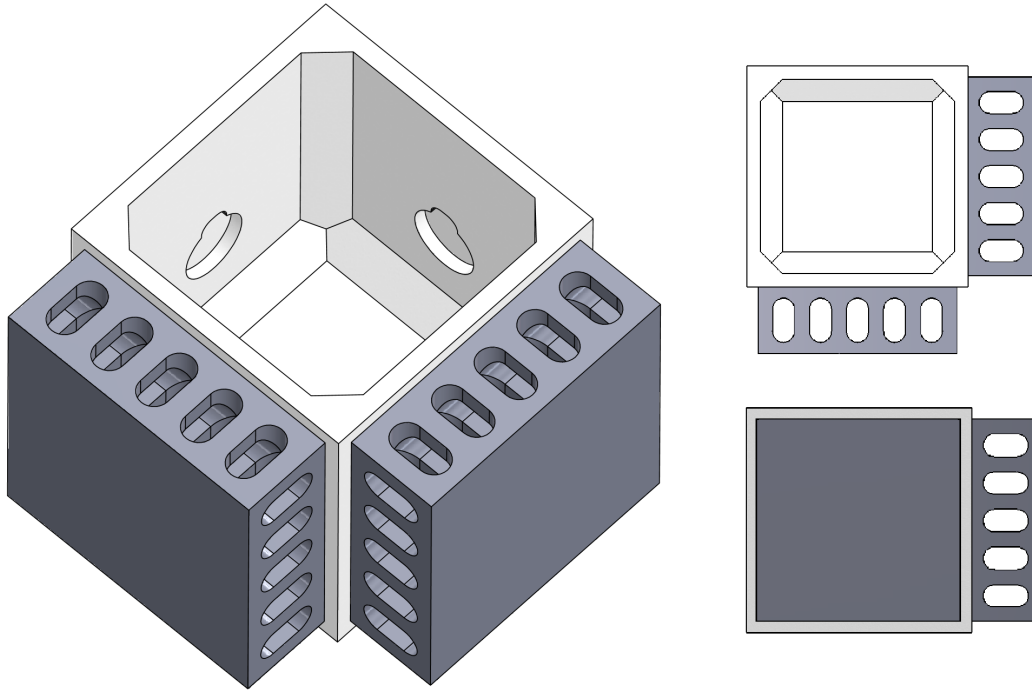


Figure 3.5: *Initial design for the cell (white) including spring elements (grey). **Top right:** Top down view. **Bottom right:** Front view.*

SolidWorks allows simulation of stresses and the resulting strains on individual parts, this allows for comparison of the stiffness and weight of potential designs before prototyping. This tool was used extensively throughout the design process and examples are included later. The first 3 prototypes are shown in Figure 3.6. The final prototype has several features to fit its design specification. Significant consideration was given to consistent construction: the extrusions on the sides of the box allow the spring elements to be precisely mated while the internal cavities allow good force transfer between components and ensure actuators and the sensing board are securely mounted in the same position every time. The parts had their mass reduced by removing material where the force simulations show low strain. Construction has also been considered allowing components to be easily removed by prying between the part and the included pry slot. While the cell could be further reduced in size, this would be at the cost of ease of assembly and force transfer between the transmission mass body and the spring element, a compromise was therefore made favouring simplicity while prototyping.

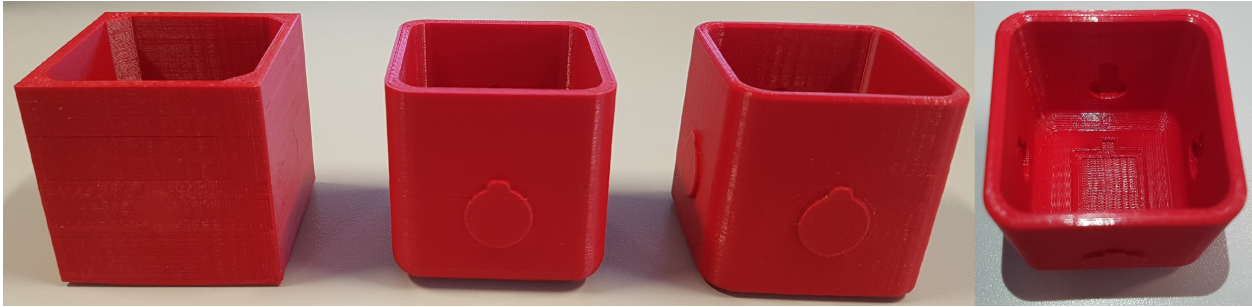


Figure 3.6: *The first 3 prototype transmission mass bodies, oldest (left) to newest (right) (shown twice).*

### 3.6.3 Manufacturing

Additive manufacture allows for production of geometries which are difficult if not impossible with traditional subtractive manufacturing. In order to reduce weight the inner sections of the object can have empty sections with only the outer faces being printed in a solid material. This hollowing to reduce weight is found in nature, often birds and sauropods have hollow (pneumatized) bones reducing energy expenditure during flight (Wedel 2005). Figure 3.7 shows a partially completed print of the transmission mass body allowing inspection of the inner structure. The lattice connecting the faces is significantly lighter than using a solid infill.

3D printers exhibit a degree of shrinkage due to the cooling of the material after it is extruded. This means that for the precise tolerances needed for a good fit, several test parts must be printed so the digital model can be adjusted. The dimensioning of the final prototype allows parts to be held in place by friction alone as shown in Figure 3.8, though a more secure fastening method was used for the final prototype.



Figure 3.7: *Image of a partially completed print showing the inner lattice between the faces of the shape.*

## 3.7 Spring Element

### 3.7.1 Design

In order to improve the applicability of the lumped model, the spring elements should have a much lower mass and stiffness than the rest of the structure, and the same stiffness in compression and extension. In keeping with the theme of development hardware, the spring was initially planned to be 3D printed in a flexible elastic material such as thermoplastic polyurethane (TPU). This would allow springs with different properties such as stiffness and length to be designed and produced on the same day. The spring constant could be adjusted very easily with no manual geometry or sizing changes, this can be done by increasing or decreasing the density of the inner lattice shown in Figure 3.7. As mentioned above the spring element was designed to interlock with the transmission mass body for easy and consistent assembly while maintaining good force. NinjaFlex was selected for the print material, as the manufacturer claims it can be printed on the same MakerBot Replicator printer as was used for the transmission mass body.

NinjaFlex typically costs £43 per spool whereas MakerBot PLA can be bought for £20 per spool, as such the initial designs were printed in PLA to test fitment and print quality before settling on the final design. Figure 3.8 shows several of the evolving prototypes and the final prototype attached to the transmission mass body by a friction fit alone. The slots between pillars were changed from an arch design to an internal chamfer because the final two layers of the top arch were unable to support themselves during printing without supports. This problem would be accentuated with NinjaFlex due to its flexibility.

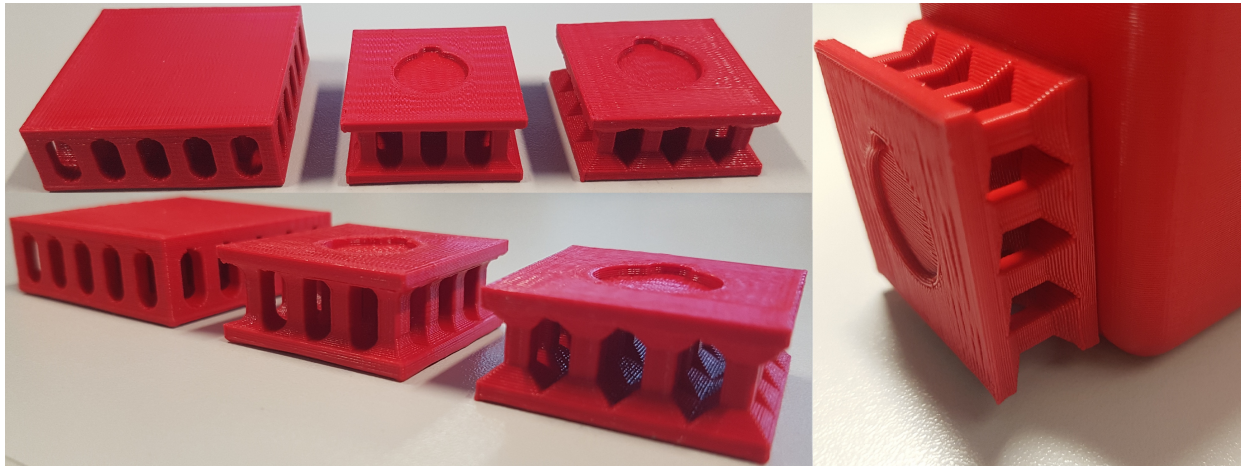


Figure 3.8: **Left:** Several design iterations for the spring element from left (oldest) to right (newest). **Right:** The final spring element design attached to the transmission mass body by friction fit alone.

### 3.7.2 Manufacturing

NinjaFlex proved challenging to print on MakerBot Replicator printers; the filament did not feed well and often wrapped around the feed driver. Many attempts were made with a variety of settings, including those recommended by the manufacturer of NinjaFlex. A part to fill the gap allowing the filament to wrap around the print head was produced; however, this resulted in the filament becoming tangled further. It was requested that the university's main production 3D printing group attempt to produce the parts, unfortunately they were unable having already destroyed six print heads attempting to print the material.

The Centre for Advanced Additive Manufacturing (AdAM) research at the University of Sheffield was contacted to help produce the parts. While not having printed NinjaFlex before they did give use of a LulzBot TAZ 4 printer capable of printing a diverse range of plastics. The Taz 4 has several print heads for specific tasks, difficult materials such as NinjaFlex require the LulzBot Flexystruder head, the retail price for this head is US\$295.00, beyond the entire project budget and was unavailable. New settings for the TAZ 4 were developed for NinjaFlex using the basic print head, this was done by repeated and careful analysis of the cause of failure for each print. Figure 3.9 shows some of the problems that were overcome to produce the final print. Table 3.1 contains the final settings that were developed and the reasoning for them. The spring element was altered to increase the minimum feature size to reduce flex during printing; however, when combined with the inability to print with an inner lattice this resulted in a much higher stiffness than was desired to maintain the lumped model approximation.

Figure 3.10 shows the best quality print that was achieved. This part still required significant finishing work and only structures larger than 4x4mm could be printed reliably. This lower bound on the size of structures that could be printed prohibited the use of an internal lattice to reduce the stiffness of the spring element, negating much of the usefulness of NinjaFlex filament for this task. The spring constant of the Ninjaflex spring element was found experimentally by compressing it with a 10KG test mass and measuring the deflection

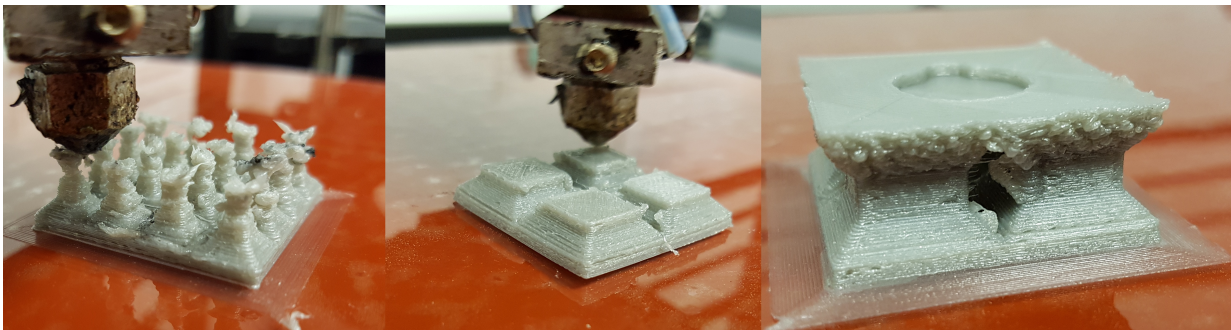


Figure 3.9: *Problems encountered printing NinjaFlex on TAZ 4: **Left:** loss of accuracy due to small structure flexing while the head prints onto them. **Centre:** Object lifting off bed due to insufficient adhesion. **Right:** Very low quality printing on overhanging portions. Note that the inclusion of a brim around the base of the object prevents lifting off.*

caused using digital calipers, the stiffness was found to be 22,333N/m. The same test was undertaken with the transmission mass body yielding a stiffness of 14,667N/m. The spring element was therefore stiffer than the transmission mass body invalidating the lumped spring assumption of the modelling.

The printed element design was replaced with a single spring and the transmission mass body modified accordingly. The replacement spring has a lower stiffness than what was achievable with NinjaFlex but could not be altered and redesigned as quickly.

Setting	Value	Explanation
Layer Height	0.3mm	Must be large to allow overhangs enough material to support themselves while being printed over.
Fill Density	100%	Unable to print at lower densities.
Printing Temperature	210 - 230°C	A high temperature must be used to make the material flow; however, this is lowered when printing overhangs to reduce droop while cooling.
Heated Bed Temperature	60°C	The bed must be hot for the initial few layers to allow the material to adhere, after this the bed is cooled.
Bed Cover	Glass	The bed must be smooth for the material to adhere properly.
Printing Speed	48mm/s	The material must be heated and cooled quickly as it rapidly degrades at temperatures high enough for smooth flow.
Support Type	None	Supports are difficult to reach for removal and when printed often collapse so do not provide any benefit.
Platform Adhesion Type	Brim	The initial layer must be larger than the base to form a good seal so that the print does not peel off while printing.
Minimum Structure Size	6x6mm	Structures smaller than this result in excessive flex causing growing errors.

Table 3.1: Final settings for printing NinjaFlex on LulzBot Taz 4.

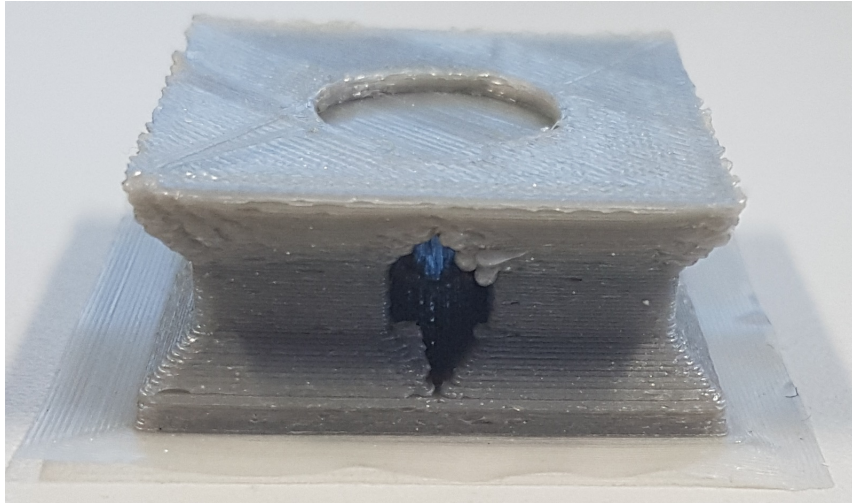


Figure 3.10: *Best quality spring element print that was achieved with NinjaFlex.*

### 3.8 Transmission Mass Body Redesign

The replacement design for the spring element required a redesign of the transmission mass body to allow for good force transfer with the spring. The replacement of the spring block with a physical spring allowed for a smaller mounting point resulting in the design being further miniaturised and lightened. The original minimum functional design has a mass of 33.92g while the redesign has a mass of 24.57g, a 27.6% reduction. This mass was further decreased to 15.98g due to the reduced material used by the internal lattice than by a solid object.

This opportunity was also used to refine the mounting point for the load cell: a recess was created on the end of the transmission mass body. This was sized precisely to allow for a friction fit giving better force transfer, holes were also added to allow the load cell to be bolted into place. The actuators were placed such that they act through the centre of mass to reduce any torques; however, the base was widened to further reduce any chance of rotation in an undesirable direction. While only one LRA is required for control in each dimension, mounting points for two per dimension are included in each cell, this allows further LRAs to be added for increased actuation force, these LRAs can be driven from the same LT1010 amplifier though their leads must be reversed so that their vibration is in antiphase as they are facing in opposite directions. Figure 3.11 shows a completed print of the redesigned transmission mass body while Figure 3.12 gives a technical drawing of the design.



Figure 3.11: *Redesign of the transmission mass body.*

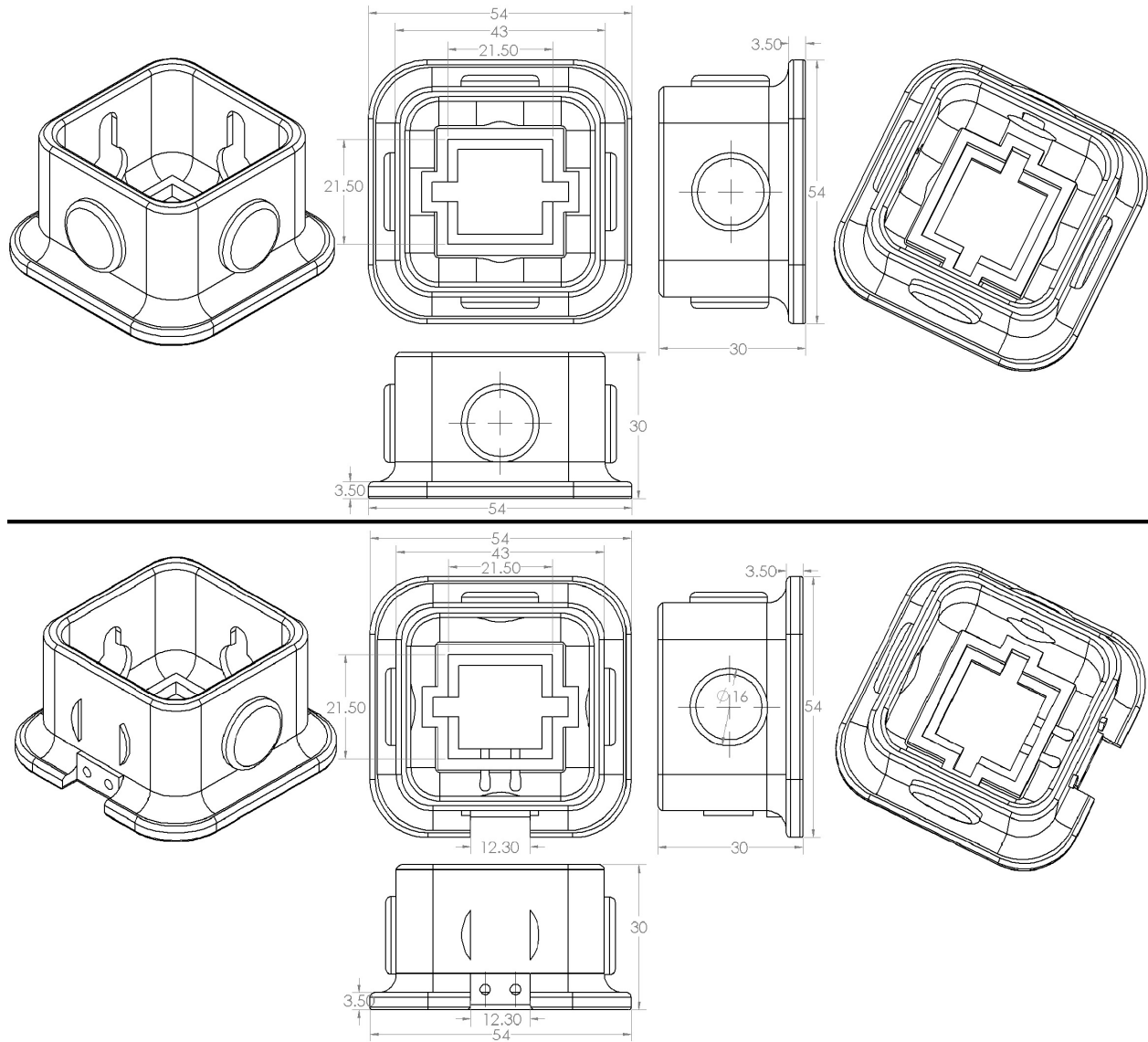


Figure 3.12: **Top:** Technical drawing of the redesigned transmission mass body. **Bottom:** Adapted transmission mass body for end cell with mounting point for load cell.

### 3.8.1 Simulation

Simulation of the old and new design was conducted in SolidWorks, a test 10Kg load was applied to one of the faces responsible for force transfer while the opposite face was fixed. Figure 3.13 shows the results of this simulation. The redesigned transmission mass body has a 28.2% lower maximum flex than the original design.

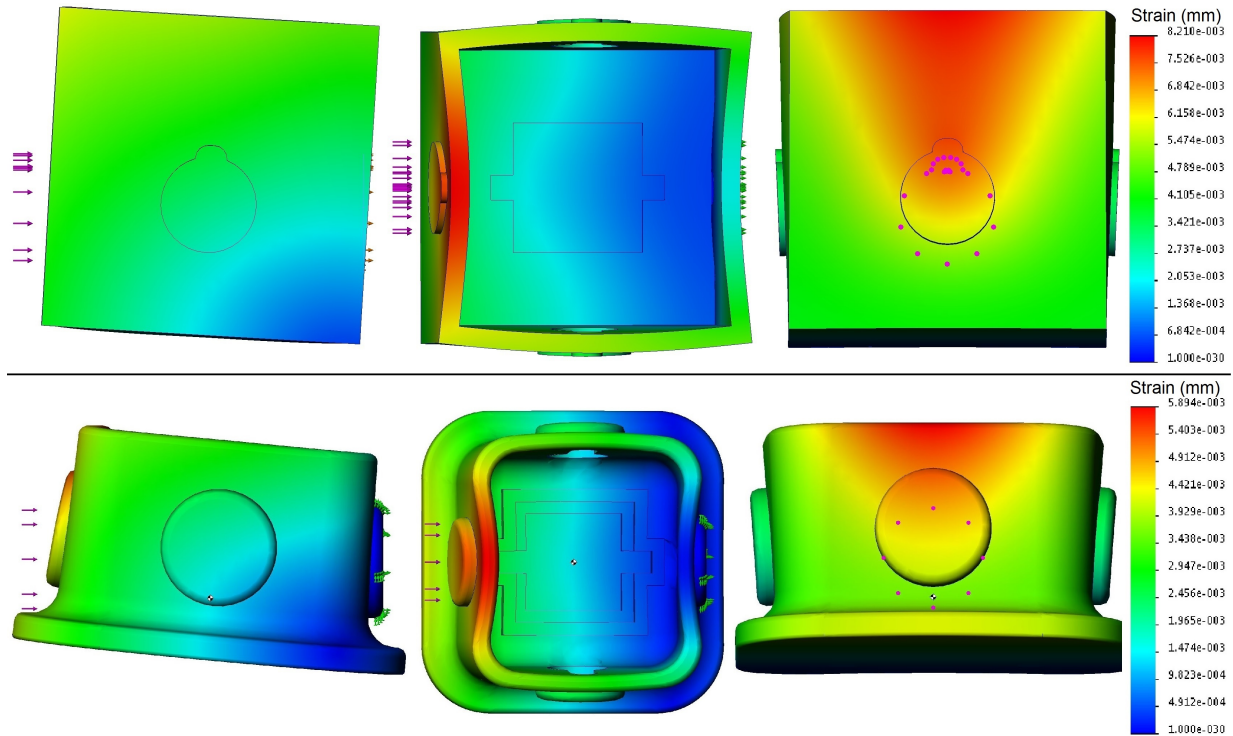


Figure 3.13: *Strain simulations of the transmission mass body designs. **Top:** Simplest minimum functional design required for using NinjaFlex. **Bottom:** Final design.*

### 3.8.2 Single Cell Assembly

Figure 3.14 shows an exploded view of the end cell assembly with all four mounting points populated with LRAs. The accelerometer is mounted to the cutout with space below given for the bottom protrusions from the I/O pins. The disturbance assembly consisting of the load cell and disturbing LRA is also shown.

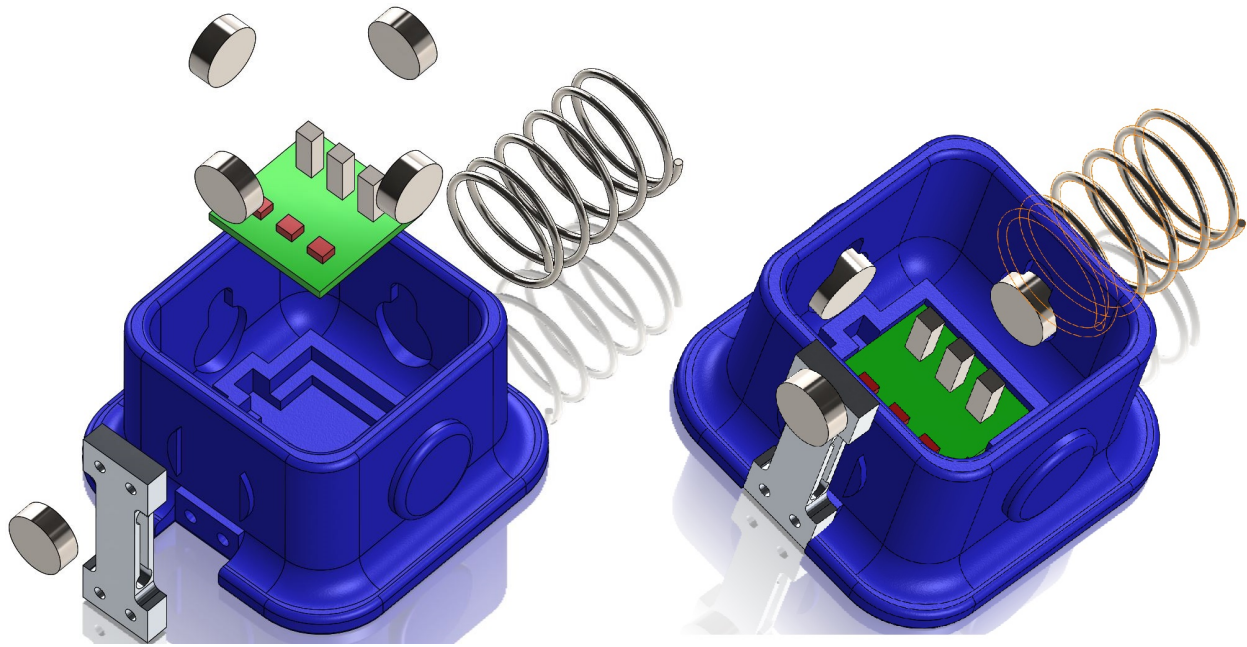


Figure 3.14: *Assembled end cell. Left: Exploded View. Right: Fully assembled.*

### 3.9 PTFE Surface Plate

It is desirable that all damping be reduced as much as reasonably practical, a significant portion of the transmission mass body's damping will come from friction with the base. A low friction base was designed to reduce this friction as much as possible. PTFE (Teflon) is well known for having an exceptionally low coefficient of friction, 0.05 to 0.10 against polished steel. This is the 3rd lowest of known solid materials and the only known surface to which a gecko is unable to stick (Liehui Ge et al. 2007). PTFE both expensive (per kilogram) and dense, CES states a typical price £9.82/Kg, as such a plywood base was produced allowing a thinner PTFE plate to be attached to the surface. Figure 3.15 shows the design for the plate and plywood base.

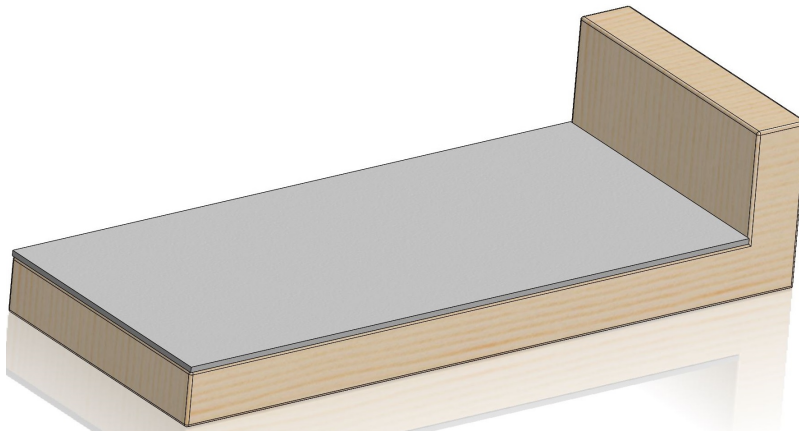


Figure 3.15: *The PTFE plate and plywood base.*

### 3.10 Full Assembly

The full assembly of a 1D array of cells is shown in Figure 3.16 and a technical drawing of the assembly is included in Figure 3.17. Though it not shown it is straightforward to see how the design can be adapted for two dimensions. Three dimensions would prove more challenging because further mounting points would be required on the top and bottom of the cell making assembly more difficult. A unibody cell could still be achieved by first partially printing the cells before assembling the internal components and then returning the part to the printer to be completed.

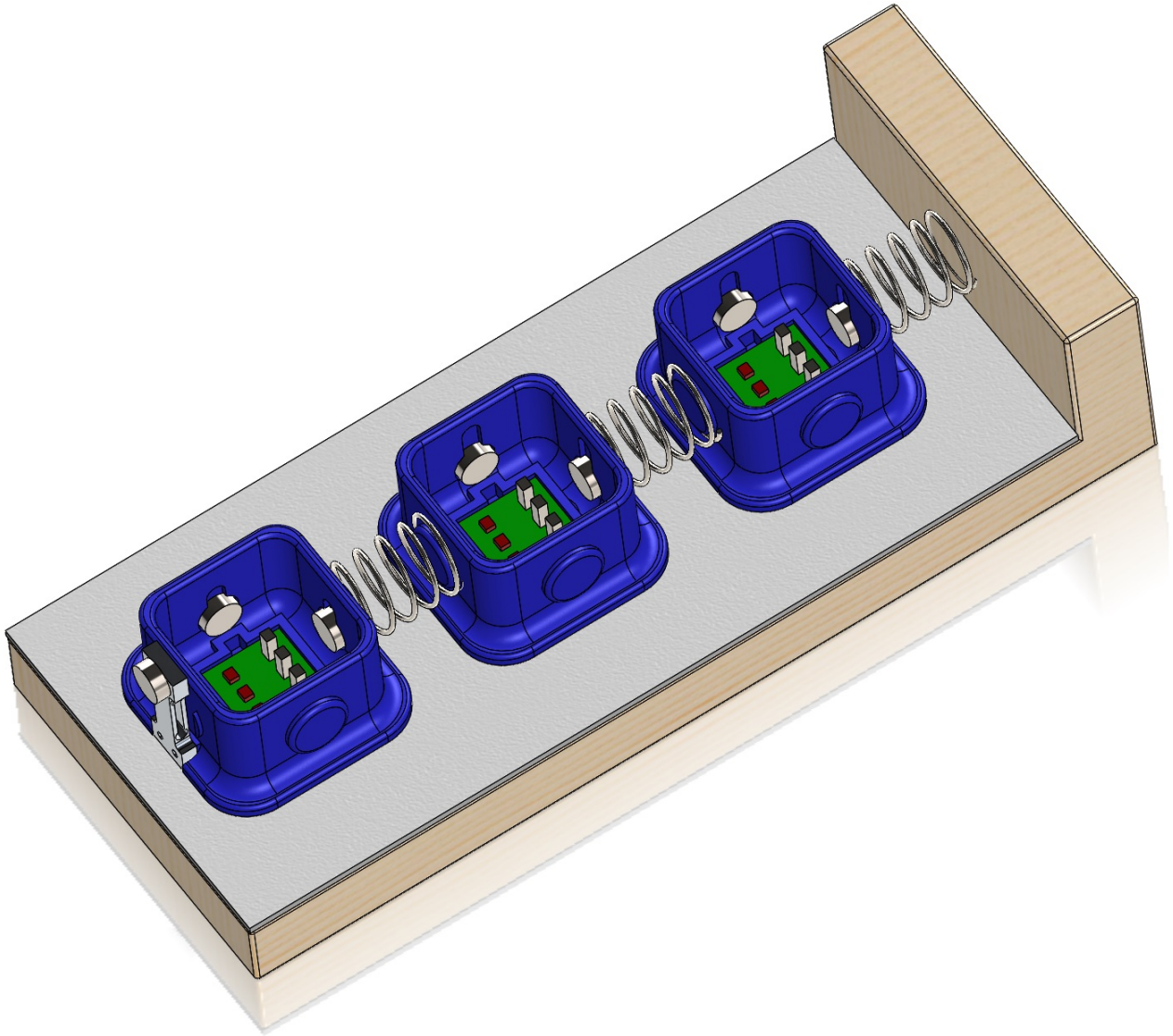


Figure 3.16: Full 1D assembly of 3 cells on the PTFE base. Accelerometers are shown in green and the LRAs are the small silver cylinders inside the transmission mass bodies.

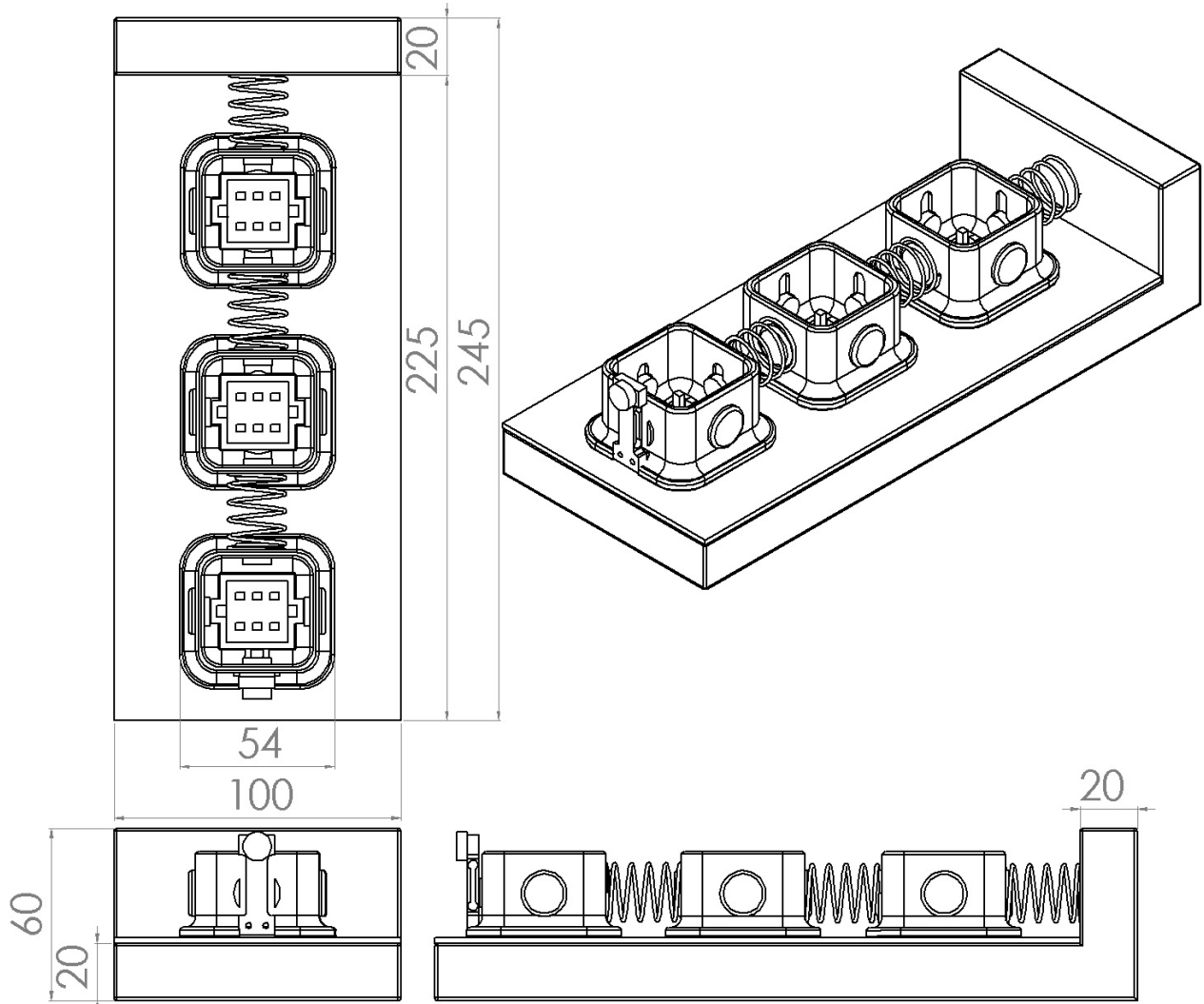


Figure 3.17: *Technical drawing of full 1D assembly of 3 cells on the PTFE base.*

### 3.11 Simulation of Design

The properties of the designed components are now known or can be derived. Masses of the components were measured using a weighing scale. A single LRA was dismantled to weigh the resonant mass, this was combined with the known resonant frequency of the actuator ( $175Hz = 1100rads/s$ ) allowing the spring constant to be approximated as  $1710N/m$ . The mass of the cells and the springs was found to be  $15.98g$  and  $4.77g$  respectively. The damping constant was found by disturbing the completed cell excluding LRAs and observing the decay of oscillations.

From the LRA data sheet the typical vibration efficiency is  $10.8 G/W$  with a  $100g$  inertial load, given the data sheet claims a  $1.5G$  acceleration with the inertial load at resonance it follows that the power consumption at resonance is  $\frac{1.5}{10.8} = 0.15W$  or  $\frac{0.15W}{175Hz} = 0.000857J$  per cycle. The data sheet quotes  $69mA$ , 'typical current' assuming this is RMS and using the

stated RMS voltage of 2V we find through  $P = IV$  that the power used overcoming the the resistor is  $0.069*2=0.138W$ , meaning the losses in the coil excluding the coil's resistance is  $0.012w$  or  $\frac{0.012W}{175Hz} = 0.0686mJ$  per cycle.

The inertial mass moves approximately 2mm peak to peak so traverses 4mm per cycle. The force produced by the voice coil can be split into force required to overcome friction and force output; however, energy is only lost from the system from overcoming friction and will appear a purely resistive load in addition to the coil resistance. Given  $\frac{work}{distance} = force$  the average force wasted overcoming friction can be estimated as  $\frac{0.0686mJ}{0.004} = 0.017N$ . Now given the mass moves 4mm in  $\frac{1}{175}s$  the average speed is 0.70m/s the losses can be calculated as  $\frac{0.017N}{0.70ms^{-1}} = 0.0244N/(ms^{-1})$ , this is the average damping of the resonant actuator mass ( $c_a$ ). Fortunately this approximation is for the free moving LRA so is separated from damping occurring outside the LRA such as transmission mass damping. This value for damping can be validated by giving a test LRA an impulse input and observing how the voltage across the terminals decays.

#### Masses

$m_t = 4.77g$	Mass of the spring.
$m_t = 15.98g$	Mass of the transmission mass body.
$m_t = 24.25g$	Total mass of the transmission body and all components.
$m_a = 1.43g$	Mass of the resonant actuation mass.

#### Stiffnesses

$k_t = 235N/m$	Spring rate of the transmission mass spring.
$k_a = 1710N/m$	Spring rate of the resonant actuation mass spring.

#### Damping

$c_t = 0.5N/(ms^{-1})$	Damping rate of the transmission mass damper.
$c_a = 0.0244N/(ms^{-1})$	Damping rate of the resonant actuation mass damper.

Figure 3.18 show the simulated frequency response of the real components of the effective mass and effective stiffness ( $m_e$  and  $k_e$ ) for the real hardware. The springs mass was lumped with the cell mass. The effective mass of the passive system achieves negativity for 4Hz around the resonant peak; however, by incorporating active control, simultaneous negativity of both  $m_e$  and  $k_e$  is achieved. The resonant peak of  $m_e$  has increased in bandwidth and depth. The  $k_{ep}$  curve has been manipulated to have similar resonant behaviour to  $m_{ep}$ . As the control gains are increased the magnitude and bandwidth of this negativity increases.

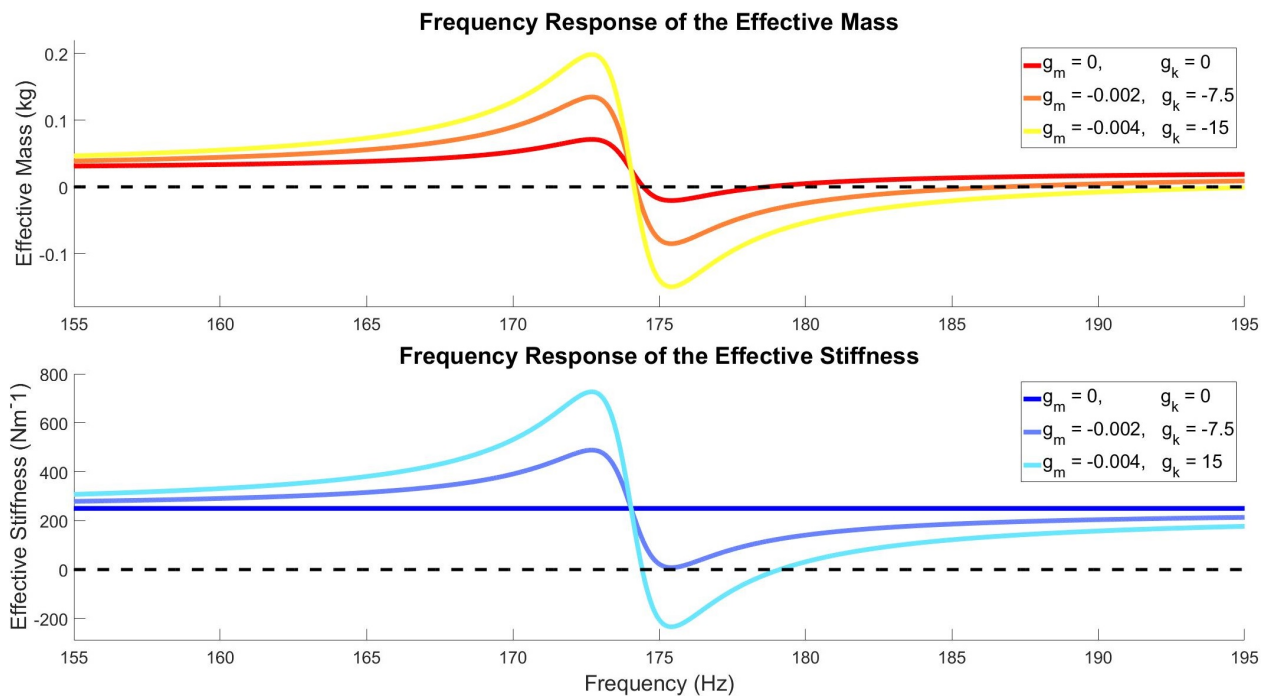


Figure 3.18: Graphs showing the simulated real components of the frequency response of the effective mass ( $m_e$ ) and effective stiffness ( $k_e$ ) for the real parameters of the active and passive system.

# Chapter 4

## Implementation, Results and Analysis

### 4.1 National Instruments LabVIEW

National Instruments LabVIEW software is designed to work with the DAQ selected for this project, as such communication between the desktop computer and the DAQ is straightforward. The LabVIEW code used to implement control and data collection is included in appendices 6.2 and 6.3.

The LabVIEW program (VI) produces a random input voltage in the range  $\pm 3V$  for the disturbing LRA, this input acts as the band limited white noise required for extraction of the effective mass and stiffness at each frequency. The inputs from the 3 accelerometers are first filtered by a 5th order Butterworth bandpass filter with upper and lower cutoff frequencies of 150Hz and 200Hz respectively. The unfiltered acceleration signals are logged in an output file along with timestamps and force recorded from the load cell.

The mass control section of the VI simply takes the filtered accelerations for each cell, multiplies them by the stiffness control gain; a sufficiently negative number to find the force required for the effective mass to become negative. The stiffness control section of the VI first performs a double numerical integration on the accelerations to determine the displacement relative to the initial position and to each other. These values are then substituted into Equation 2.9 to find the force required for negative stiffness.

The mass and stiffness force requirements are then summed and coerced to stay within the operating range of the LRAs ( $\pm 2V$ ) before being outputted to the DAQ. This implementation does not include the actuator dynamics that were derived in section 2.5.2.

### 4.2 Sampling

It was found very late in the project that the available PC was unable to run the controller sufficiently fast to stay synchronised with the DAQ, this resulted in slowdowns and dropped samples. This presented a significant issue as constant sample periods were required for the analysis of the results. This was not easily predicted as the computational cost of the control

and logging program was unknown until after the program was completed, especially in a high level programming language such as LabVIEW. In order for the actuators to run at peak force output (175Hz) the resulting oscillations must be captured at a minimum of the Nyquist frequency to avoid aliasing (350Hz) giving a maximum period of 2.8ms.

LabVIEW only allows the period of the program to be adjusted to whole millisecond increments, meaning the maximum acceptable program period is 2ms as 3ms would fail to meet the Nyquist frequency. The first version of the control and logging program saved the samples to file at the end of every cycle. This results in unnecessary slowdown as hard disk drive access is relatively slow, the program was altered to save all captured data to a memory buffer and only writing the contents of this buffer at the end of the program. This greatly reduced the period of the program as random access memory (RAM) found in desktop computers typically has a write latency of below 20ns. Unfortunately even when writing to memory the program was unable to execute sufficiently quickly. The stiffness control section of the program has a significant computation expense as double integration is required for each accelerometer to calculate displacement. For this reason the stiffness control portion of the program was dropped in favour of focusing on active mass control.

The sample rate at which the program was able to reliably log data was found experimentally to be 500Hz, the disturbing frequency was therefore lowered to 100Hz because, while possible to extract true dynamics from a signal up to 250Hz, practically this is difficult at the limits of the Nyquist frequency. Typically sampling at ten times the highest frequency present in the signal is desired. Moving away from the resonant frequency of the LRAs reduced the output force of the disturbing LRA and therefore the signal to noise ratio from the accelerometers; however, the force and resulting accelerations were still detectable. The length of data collection was increased from 60s to 150s which, assuming zero mean noise, allows more of the noise to be cancelled out during analysis.

### 4.3 Test Setup

Figure 4.1 shows the experimental setup used for collection of data. The PTFE Surface plate was placed on a thick open cell foam pad to reduce external vibration. The silver faced power supply supplies 3V to the accelerometers as the potential divider on the AD623 board is unable to supply sufficient current while maintaining 2.5V. The black faced power supply supplies  $\pm 5V$  and ground to the LT1010 power rails. The NI-cDAQ-9178 CompactDAQ Chassis can be seen in the top of the Figure with the NI-9201 Input module and NI-9263 output modules populating slots 1 and 2 respectively.

The LabVIEW program outputs a comma separated variable (.csv) file with the timestamps, loadcell force and accelerations of each of the three accelerometers. This data requires processing before any meaningful results can be identified.

Data was collected with both positive and negative control gains as the polarity of the LRAs was unknown, as such until the collected data was analysed it was difficult to tell if the controller was increasing or decreasing the effective mass. It was found that with the red LRA wire attached to the LT1010 output a negative control gain gave the correct phasing.

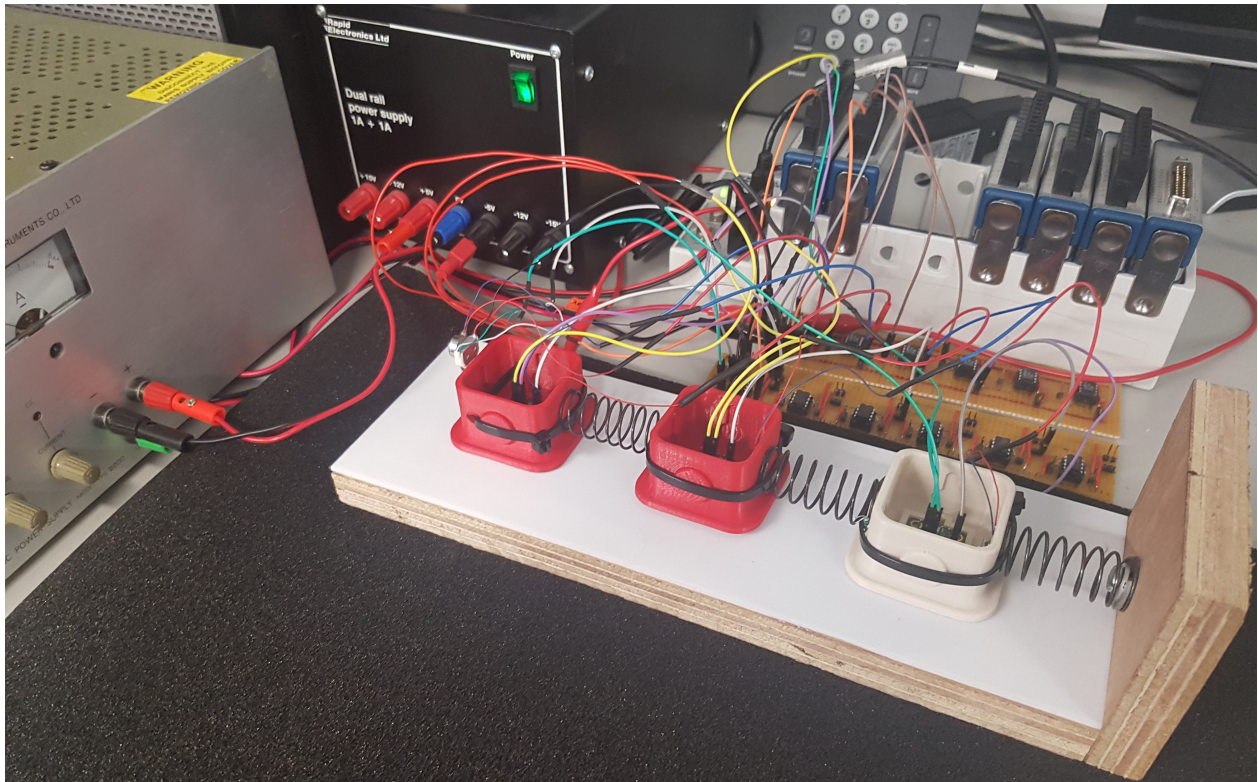


Figure 4.1: *Experimental setup used for capturing data.*

## 4.4 Data Processing and Results

Figure 4.2 gives an example of the data that was captured experimentally, very little can be ascertained from the data without significant processing. As in Pope (2014) grey box systems identification was used to extract real and imaginary components of the effective mass and stiffness from the time series data across the frequency band of interest.

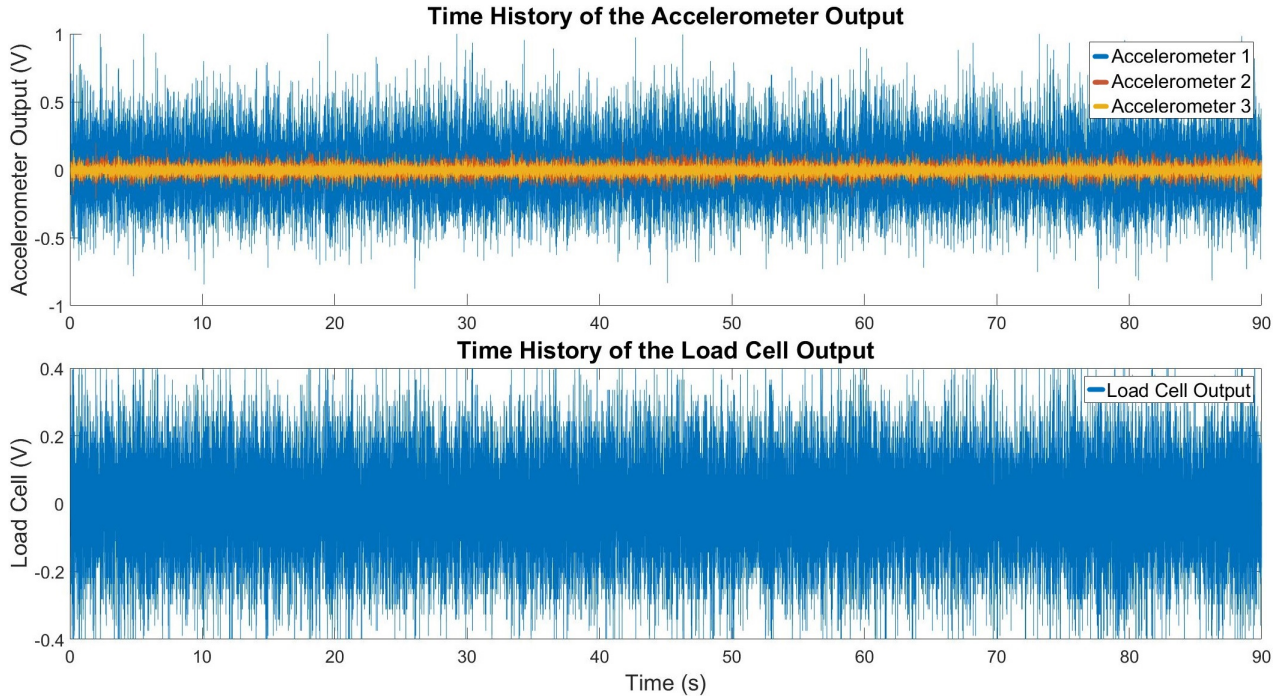


Figure 4.2: *Example of the time history of the accelerometer and load cell signals generated experimentally.*

### 4.4.1 Passive System

Figure 4.4 gives the experimental results for the passive transmission mass system and the full system including the LRA's resonant masses. The LRAs were disconnected from the control board giving an open circuit resistance between the two leads. This was done to prevent the induced EMF, from the vibrating resonant masses producing a current and therefore magnetic field which would alter damping. The same program was used for both the passive and active system with only the control gains being altered. Irregularities in the sample rate may be caused by the control algorithms being more computationally expensive than just data collection. These irregularities could cause a frequency shift making comparison of results difficult.

Both the transmission only and full system plots display the resonant behaviour expected, this shows that the damping is sufficiently low. The real component of the resonant behaviour is due to the actuator mass within the LRAs resonating, whereas the imaginary term (not shown) constitutes the loss within the system due to damping.

The full system's resonant peak is of greater amplitude and slightly lower frequency than the transmission only system. However, it is unusual that the transmission only system has a resonant peak at all; the system should have a flat response across the entire frequency range. There are several possible reasons for this unexpected behaviour: the systems identification algorithm used to extract the effective mass and stiffness assumes the properties of each cell are homogeneous and that parameters are lumped, that is the spring is massless and the transmission mass body does not flex. The springs make up 19.6% of the mass of the system; however, the spring with the fixed attachment to the PTFE plate will be partially supported and unable to move at one end. Additionally some vibration will propagate from the transmission mass bodies through the PTFE plate and through the fixed spring which may cause unexpected behaviour. Similarly the stiffness plots for the passive system should be flat; however, they also display resonant behaviours.

The simulation results and experimentation results display similar magnitude effective mass peaks and troughs. The passive simulation peak occurs at 173Hz and has a magnitude of 7g, experimental results also show a peak at 173Hz with a magnitude of 6.7g. The passive simulation trough occurs at 175.3Hz and has a magnitude of -2g whereas the experimental results show a trough at 178.5Hz with a magnitude of 3g. The full system displays a similar negative effective mass bandwidth as the simulation of approximately 3Hz though it is slightly shifted upwards in frequency. This frequency shift could be an artifact of the low sampling rate as discussed above. The good agreement between the simulation and experimental results indicate that the model parameters are reasonably accurate.

Both the transmission and full system display short periods of double negativity; however, for the effective stiffness this is most likely because of the massive spring acting to invalidate the lumped parameter assumption used to extract stiffness, as discussed above, rather than actual negativity.

The high frequency resonance at 187Hz again appears to be caused by the massive springs. This is because the spring mass gives them their own resonance. The massive spring can be modelled as shown in Figure 4.3 where  $K_t$  is the stiffness of the spring and  $M_s$ . The masses can be assumed to be lumped in the spring as spring-mass-spring, the resulting springs are twice as stiff so give higher frequency resonance.

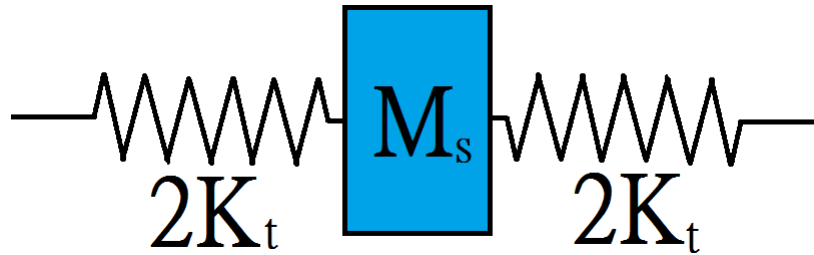


Figure 4.3: *Lumped model of massive spring.*

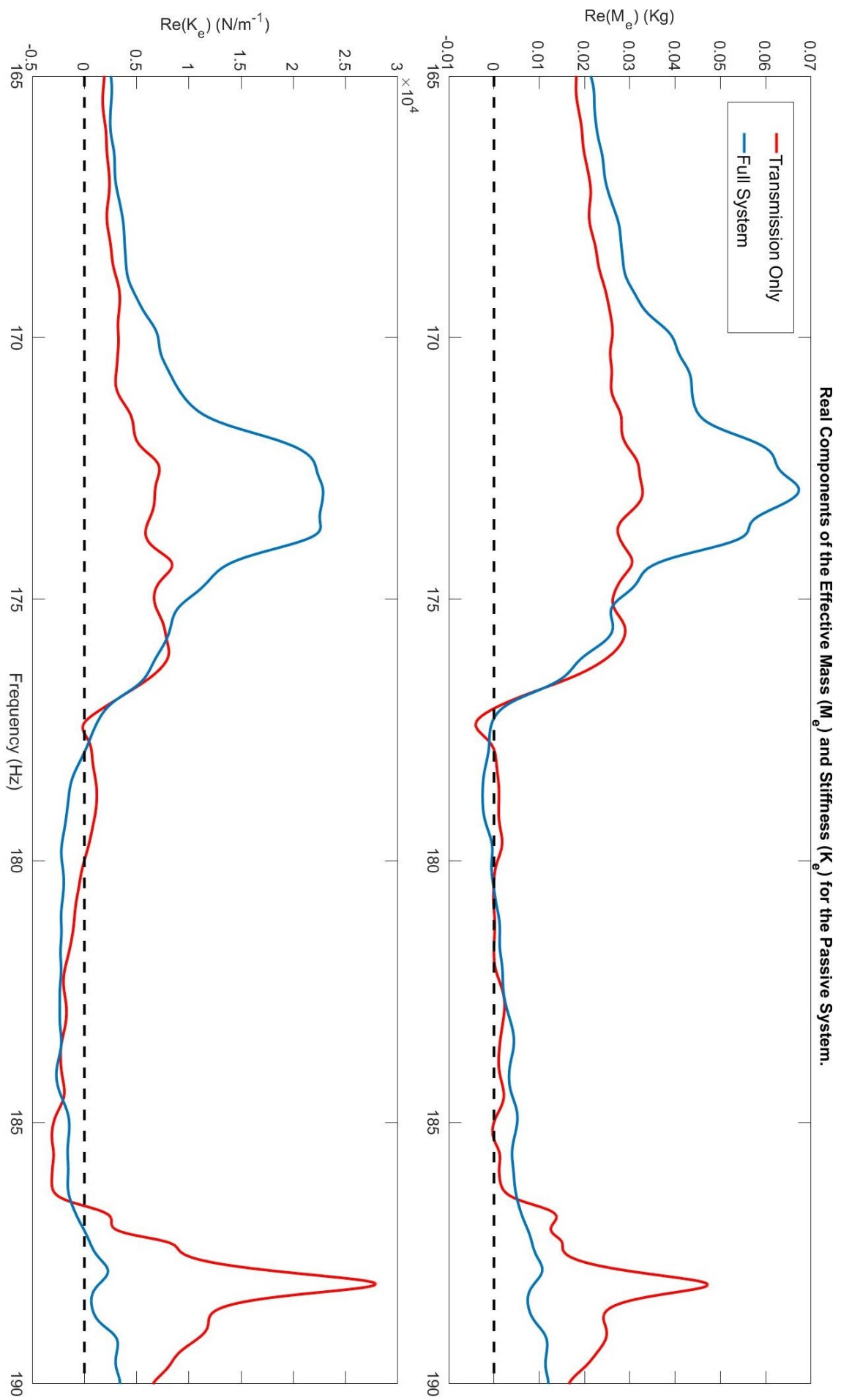


Figure 4.4: *Experimental results for the transmission only and full passive system.*

## 4.4.2 Active System

Figure 4.5 shows the experimental responses of the system with both positive and negative gain, it is clear that the negative gain results in the deeper negative trough with broader bandwidth showing the control to be effective. This plot was used to identify the phasing of the LRAs.

Figure 4.6 gives the experimental results for the actively controlled system. Implementation of the mass control law has improved both the depth and bandwidth of the negative region. It is interesting to note that decreasing the control gain from -1 does not seem to have produced a deeper trough; however, -4 was the most negative the control gain could be in order to remain stable. This suggests that the actuators are already acting to their maximum potential with a gain of -1 and increasing the gain further does not have any effect until the system becomes unstable. This hypothesis can be tested by populating the second LRA position allowing for greater actuation force or by plotting the voltage-force relationship at the frequency of interest. Increasing control gains resulted in the resonant peak having a lower magnitude before the resonant trough, this same behaviour was seen in Pope's (2014) actively controlled system plots, unlike the simulation result.

Negative effective mass is achieved between 176.3Hz and 185.1Hz with a peak negativity of -7.61g at 178Hz. This is a peak negativity representing 31.4% of the true mass of the transmission system. The plots show a negative effective stiffness between 177.5Hz and 190.5Hz with a peak negativity of  $-3675\text{N/m}^{-1}$  at 183.4Hz, though as discussed before this negative stiffness may be an artefact of a flaw in the data processing rather than true negativity.

Further analysis of the execution time of the program give interesting results; because the computer was unable to read output data in less than 2ms periods while the system itself was operating at 10ms periods with two direction changes per cycle. This means that for up to 40% of the time the control signal sent to the LRA may be delayed and therefore act against the actual desired output; however, practically the average is likely closer to 20%. It is well known that delays often degrade the performance of systems. It seems likely that by running the control on a faster computer capable of sampling and controlling more quickly would not only allow for increased force output from the LRAs and the double integration required for stiffness control, but would also improve the performance of the mass control algorithms.

The time series graph (Figure 4.2) shows that transmission mass body 1 experiences far more vibration than 2 and 3. The lower magnitude of vibration for accelerometers 2 and 3 may suggest that a higher control gain could be used for their respective controllers to improve performance. This was found not to be the case. Increasing these control gains actually degraded performance, however this may be due to the homogeneous cell assumption for the mass and stiffness extraction algorithm. This should be tested again in future when more refined algorithms have been developed allowing for heterogeneous cell properties.

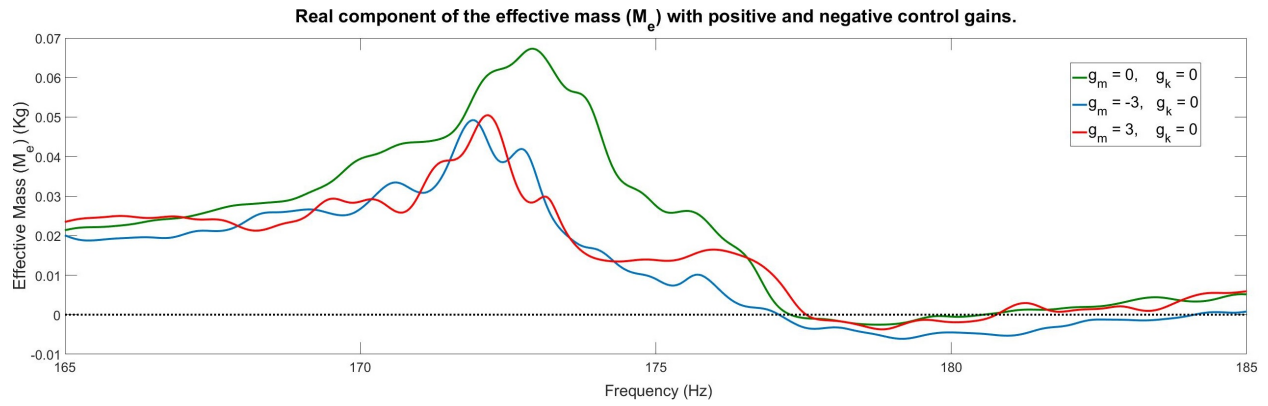


Figure 4.5: *Experimental results for the passive system and the active system with both positive and negative gains. It is clear that the negative gain produces a deeper and wider resonant trough.*

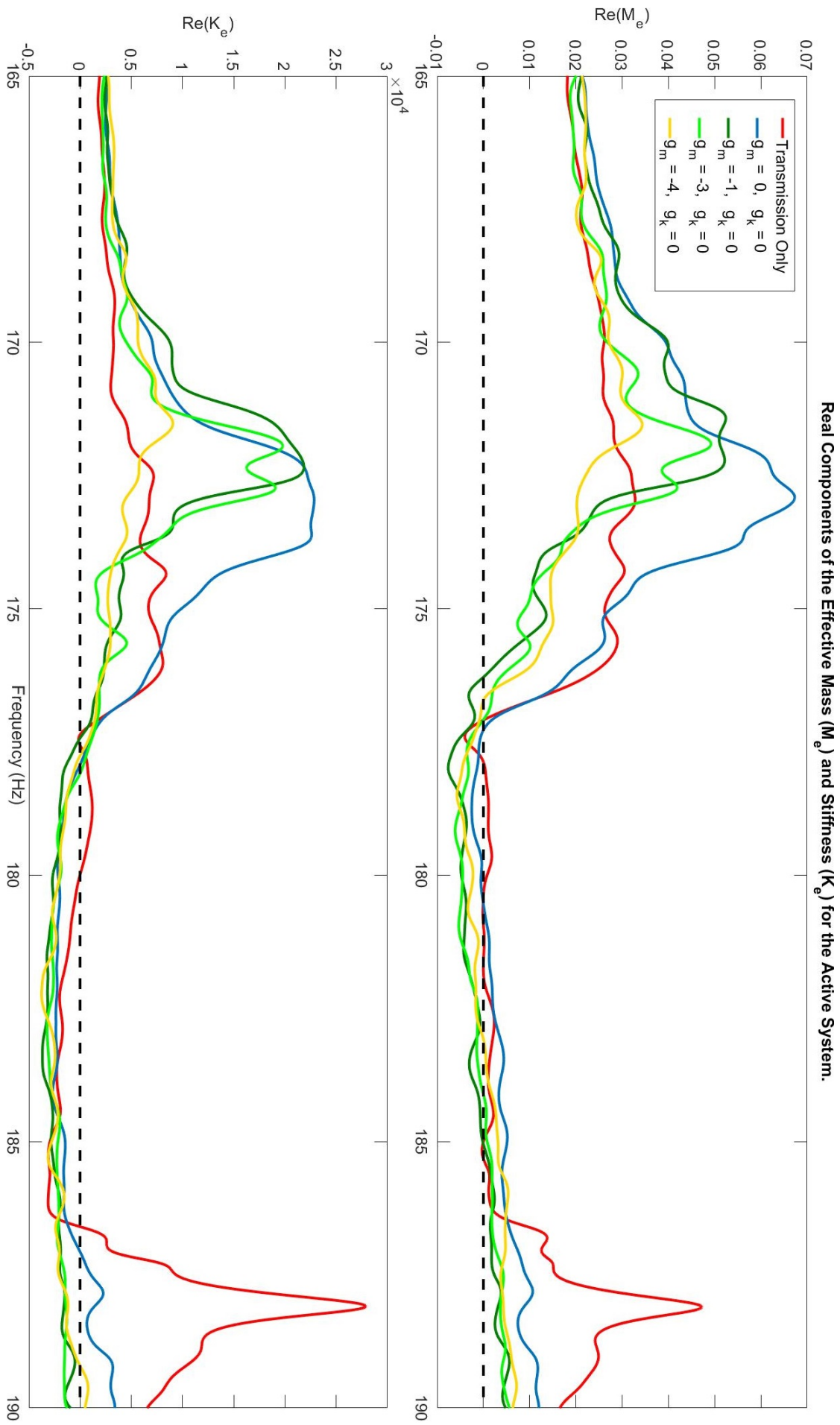


Figure 4.6: *Experimental results for the actively controlled system at various gains.*

# Chapter 5

## Conclusion

An extensive literature review on the broader topic of wave manipulating metamaterials and on the specifics of actively controlled metamaterials for vibration cloaking has been undertaken. This literature review identifies the common themes between separate papers and describes how this project seeks to fill gaps in current understanding.

Control algorithms for manipulation of the effective stiffness and mass of a mechanical metamaterial have been demonstrated successfully in simulation. The control algorithm for active control of effective stiffness was derived and coded in LabVIEW, unfortunately implementation on hardware was unsuccessful due to insufficient computing power to consistently reach the required sample rate. The mass control law has been applied to experimental hardware yielding the expected result.

Bespoke hardware has been developed to allow for miniaturisation and generalisation to two dimensions of previous work (Pope 2014). As far as the author is aware, this hardware is the smallest load-bearing, actively controlled metamaterial capable of achieving negative effective mass in the current research literature.

### 5.1 Future Work

One of the primary goals of this project has been to produce a set of development designs suitable as a platform for future research. Several small changes could be made to the hardware to improve the results of future experimentation.

The results discussed above were achieved with the minimum number of LRAs possible, that is one per cell and one providing the disturbance force; however, the transmission mass body has been designed to take up to four LRAs in total with up to two in any dimension. By populating the provided slots with an additional LRA per dimension would allow for a greater force output and consequently a higher signal to noise ratio.

The current transmission mass body design includes a flared base to reduce the possibility

of roll caused by forces not acting through the centre of mass. It was found during the experimentation that this was unnecessary, as such it could be removed from the hardware design further saving weight (approximately 15%).

The current setup could be implemented on a faster computer capable of completing the double integration required for active stiffness control to achieve double negativity. Additionally the accuracy of the control forces could be improved by implementing the force voltage relationship that was derived.

Some experimentation with different control gains for each cell were done; however, because of the homogeneity assumption for mass and stiffness extraction, it was challenging to extract meaningful information from these data sets. Improving this extraction algorithm would allow for further research in this area. Additionally with an improved model it may be possible to incorporate the elasticity required into the transmission mass body itself, rather than a separate spring element.

The imaginary term in the effective mass and stiffness equations represents loss in the system, these terms are also extracted alongside the real values. It is likely that some algorithm could use the imaginary terms to estimate damping within the system.

Finally, the hardware could be used to expand the 1D algorithms to a 2D implementation. This would require the inclusion of a third resonance over the 1D implementation, though this should be passable by including a rotation about the vertical axis in the current hardware.

## **5.2 Progress Against Aim and Objectives**

### **5.2.1 Aim**

The aim of designing, simulating, constructing and testing a unit cell with control, sensing and actuation sufficient to have both negative effective density and elasticity when part of a homogeneous pattern of unit cells has been largely completed; the test section for negative elasticity was not completed due to problems described above. The cell was designed to be capable of operation in two dimensions, without the use of fixed points and reactive actuation though this was not tested as it falls outside the scope of this project.

### **5.2.2 Basic Objectives**

1. A literature review on passive and active mechanical metamaterials and effective design from a sensing, actuation and topology perspective.
2. Component characteristics required for double negative behaviour have been identified and tested.

3. An easily repeatable design for the unit cells for both 1D and 2D arrays has been developed. This design can be used as a platform for the future work discussed above.

### 5.2.3 Advanced Objectives

1. Control algorithms capable of producing the double negative behaviour in one dimensional arrays have been developed.
2. The performance of both the passive and active designs have been simulated and analysed in 1D.
3. Three unit cells have been constructed.
4. The performance of a 1D cell array for the transmission only and passive system have been tested and analysed, additionally the active mass control algorithms have been validated.

All basic objectives have been completed. All advanced objectives have been completed with the exception of validating stiffness control algorithms on the test hardware; however, these algorithms were demonstrated as effective in simulation. Objectives identified as beyond the state of the art have not been completed. Significant effort has been devoted to the production of a hardware design which is both scalable and easily modified allowing future work to be undertaken on areas outside the 1D scope of this project.

## 5.3 Project Management

The literature review was completed early; however, due to the challenging nature of this project a large amount of time was spent understanding the problem and potential solutions. Significantly more time was required for the modelling than was initially expected, much of the work is counter intuitive and the mathematics must be trusted. Additionally several weeks were spent developing and testing methods of printing NinjaFlex, when this design was abandoned much design had to be repeated. These two factors resulted in lagging behind the planned progress as indicated by the Gantt chart (Figure 5.1). It should be noted that the original Gantt chart represented a best case and highly ambitious scenario with much of the second semester devoted to very challenging work representing a significant and novel contribution to the field.

### Budget

Table 5.1 contains a list of components used for this project and their cost. Many of the parts such as the accelerometers and LRAs were purchased before this project and were therefore not deducted from the budget. The total budget for this project was £200, the total spent was £70.68 (35%). The total cost of equipment used excluding tools was £2261.16 though £2020 (89%) of this was accounted for by the DAQ, which was used due to availability and could be replaced with a much less expensive model with no performance loss in this case.

<b>Items Purchased</b>	Number	Cost	Total
Analog Devices AD623ANZ	10	£2.94	£29.40
Linear Technology LT1010	10	£3.33	£33.3
PTFE Sheet 100mm x 300mm	1	7.98	£7.98
<b>Total Spent</b>			£70.68
<b>Additional Items Used</b>			
Precision Microdrives C10-100 LRA	5	£6.38	£31.9
Analog Devices ADXL327	3	£35.85	£107.55
Phidgets 100g Micro Load Cell	1	£7.00	£7.00
Single Sided Veroboard 111 x 176	0.5	£6.95	£3.47
Miscellaneous Electronic Components	100	£0.01	£1
Model Truck Suspension Springs	4	£2.5	£10
PLA 3D Printer Filament	0.22	£20	£4.4
NinjaFlex 3D Printer Filament	0.12	£43	£5.16
NI-cDAQ-9178 CompactDAQ Chassis	1	£1,230	£1,230
NI-9201 Voltage Input Module	1	£395	£395
NI-9263 Voltage Output Module	1	£395	£395
<b>Total</b>			£2261.16

Table 5.1: Items purchased and used for project.

# Project Gantt

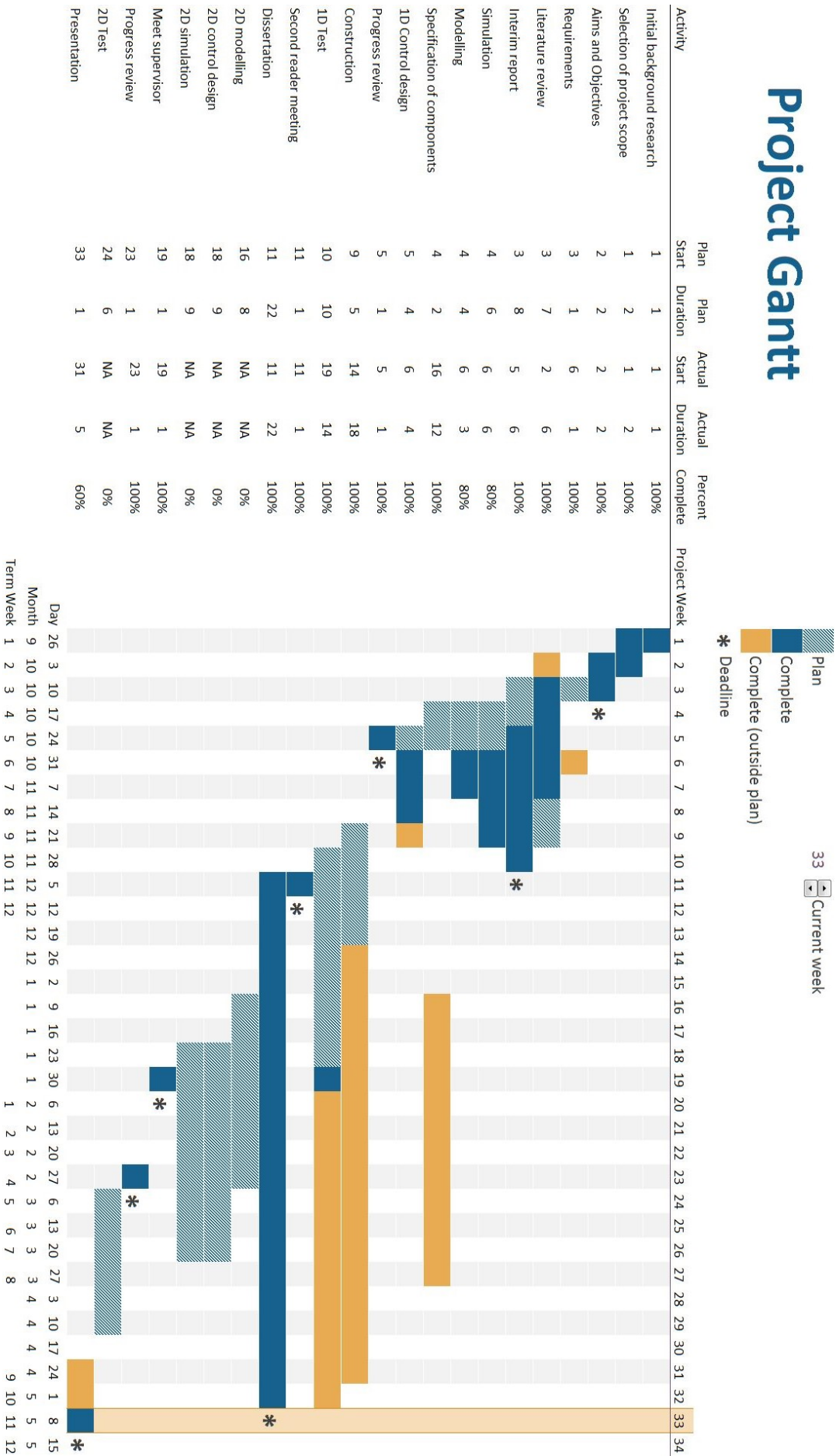


Figure 5.1: Gantt chart indicating progress against the planned work program.

# Chapter 6

## Appendices

### 6.1 Appendix A: MATLAB code used to simulate effective mass and stiffness.

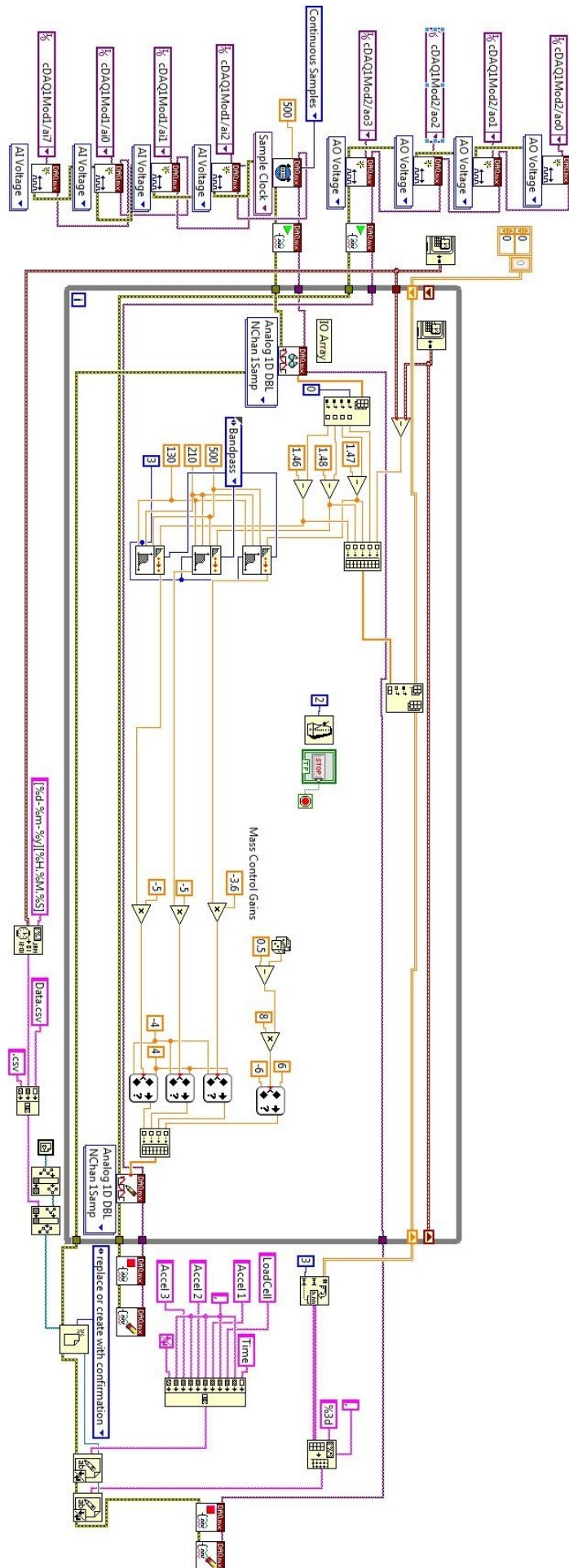
```
1 % Theodore Abbott 2016
2 % Program to find the effective mass and stiffness across the frequency
3 % range specified for the active and passive systems.
4
5 close all
6 clear all
7 clc
8
9 m_t = 24.25*10^-3; % Total transmission mass (Kg)
10 c_t = 0.5; % Damping of the transmission mass (N/(m/s))
11 k_t = 250; % Stiffness of the transmission mass springs (N/m)
12
13 m_a = (1.43)*10^-3; % Total actuation mass (Kg)
14 c_a = 0.0244; % Damping of the actuation mass (N/(m/s))
15 k_a = 1710; % Stiffness of the actuation mass springs (N/m)
16
17 m_f = -0.004; % Mass control gain
18 k_f = -15; % Mass control gain
19
20 % Frequency range to simulate over (rads/s)
21 w = 130*2*pi:0.001*2*pi:250*2*pi;
22
23 % Passive system mass
24 m_e_p = m_t + (c_a*w*li*m_a + k_a*m_a)./(m_a*(w*li).^2 + c_a*w*li + k_a);
25
26 % Passive system stiffness
27 k_e_p = k_t + (c_t*w*li);
28
29 % Active system mass
30 m_e = m_t + m_a*((m_f*(w*li).^2 + c_a*(w*li) + k_a)./(m_a*(w*li).^2 + c_a*(w*li) + k_a));
31
32 % Active system stiffness
33 k_e = c_t*(w*li) + k_t + (m_a*k_f*(w*li).^2)./(m_a*(w*li).^2 + c_a*(w*li) + k_a);
34
35 % Plotting Results of effective mass
36 figure
37 subplot(2,1,1)
38 hold on
39 plot((w./(2*pi)), m_e_p, 'r', 'LineWidth', 6); set(gca, 'FontSize', 22)
```

```

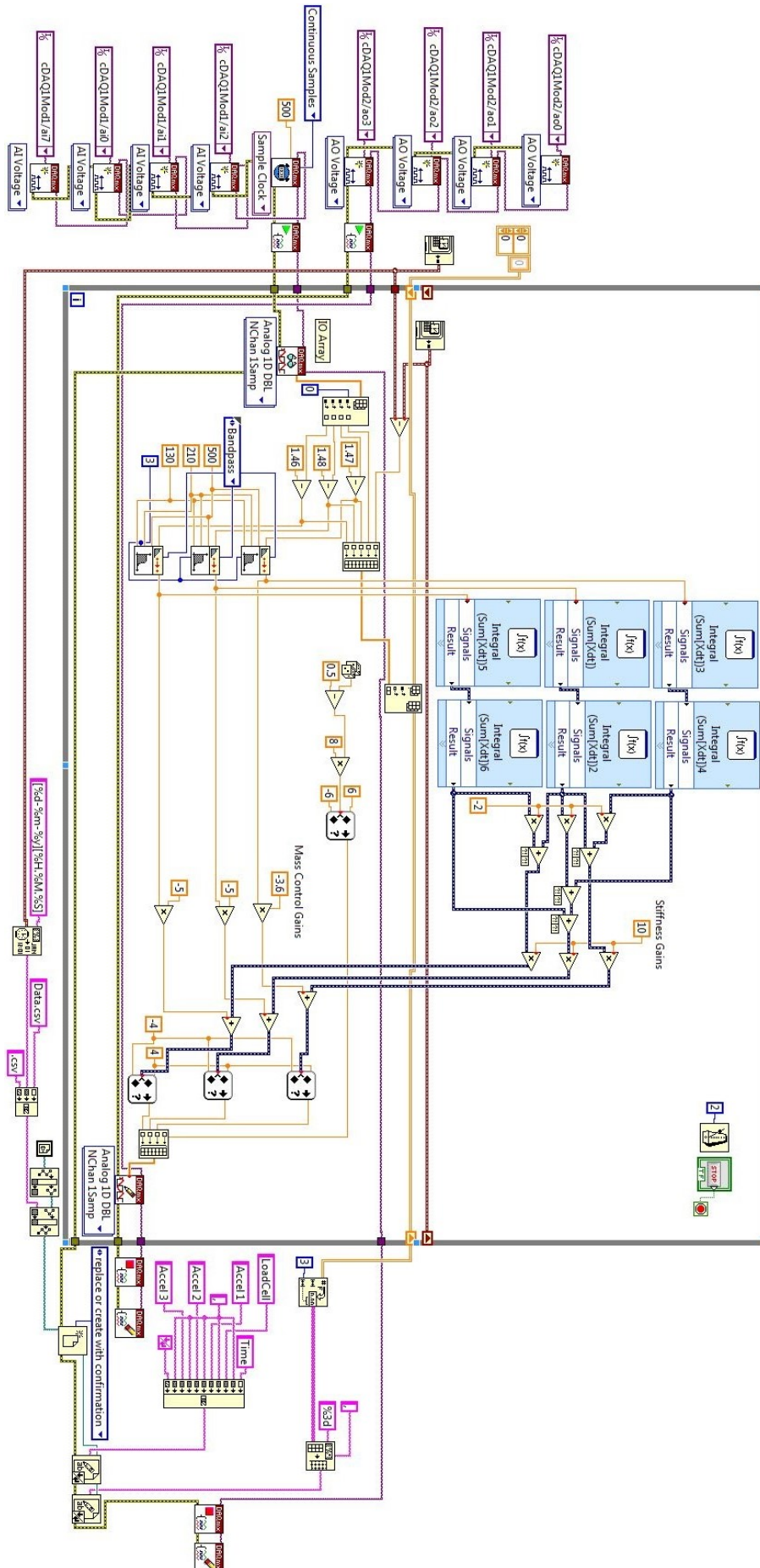
40 plot((w./(2*pi)),m_e,'-','LineWidth',6);set(gca,'FontSize',22)
41 plot((w./(2*pi)),ones(size(w))-1,'LineWidth',4,'color','k')
42 title('Frequency Response of the Effective Mass','FontSize',30)
43 ylabel('Effective Mass (kg)','FontSize',28)
44 axis([150 200 -0.2 0.2])
45 h_legend = legend('Effective Mass of the passive system.','Effective Mass of the ...
    active system.','Effective Mass = 0','Location','northeast');
46 set(h_legend,'FontSize',28)
47
48 % Plotting Results of effective stiffness
49 subplot(2,1,2)
50 hold on
51 plot((w./(2*pi)),k_e_p,'LineWidth',6,'color','magenta');set(gca,'FontSize',22)
52 plot((w./(2*pi)),k_e,'-','LineWidth',6,'color','cyan');set(gca,'FontSize',22)
53 plot((w./(2*pi)),ones(size(w))-1,'LineWidth',4,'color','k')
54 title('Frequency Response of the Effective Stiffness','FontSize',30)
55 xlabel('Frequency (Hz)','FontSize',28)
56 ylabel('Effective Stiffness (Nm-1)','FontSize',28)
57 axis([150 200 -300 800])
58 g_legend = legend('Effective Stiffness of the passive system.','Effective Stiffness of ...
    the active system.','Effective Stiffness = 0','Location','northeast');
59 set(g_legend,'FontSize',28)

```

## 6.2 Appendix B: LabVIEW code used to for experimental mass control.



## 6.3 Appendix C: LabVIEW code used to for experimental mass and stiffness control.



## 6.4 Appendix D: Progress Report 1



The  
University  
Of  
Sheffield.

Automatic  
Control &  
Systems  
Engineering.

### ACS420: Individual Project – Progress Review Form

**Student name:** Theodore Abbott (120139831)  
**Project code and Title:** Robotic Materials (SAP1)  
**Supervisor:** Dr Simon Pope  
**Second Reader:** Dr George Konstantopoulos

#### Project progress against objectives:

- Initial background research has been completed.
- Selection of project scope has been completed.
- Aims and Objectives have been completed.
- Requirements Document has been started, however it is still a first draft and will require much more work.
- Literature review has been largely completed. Time needs to be spent researching the best shape for the unit cells.
- Interim report has been started but still requires a lot of work. It will largely cover the literature review, initial modelling and design.
- Simulation has not yet been started.
- Specification of components has not yet been started.
- Modelling has not yet been started.
- 1D Control design has not yet been started.

#### Main tasks to be completed in the next 4 weeks:

- Complete the requirements document.
- Complete initial literature reviews to inform the design.
- Begin initial modelling and simulation of the system to inform specification of components.

**Student name:** Theodore Abbott 02/11/2016

**Supervisor:** Dr Simon Pope SAP 02/11/2016

## 6.5 Appendix D: Progress Report 2



The  
University  
Of  
Sheffield.

Automatic  
Control &  
Systems  
Engineering.

### ACS420: Individual Project – Progress Review Form

**Student name:** Theodore Abbott (120139831)  
**Project code and Title:** Robotic Materials (SAP1)  
**Supervisor:** Dr Simon Pope  
**Second Reader:** Dr George Konstantopoulos

#### Project progress against objectives:

- Initial background research has been completed.
- Selection of project scope has been completed.
- Aims and Objectives have been completed.
- Requirements Document has been completed.
- Literature review has been largely completed.
- Interim report has been completed
- Modelling, simulation and control design for 1D behaviour and deformation of the structure has been completed.
- Specification of components is partially completed, some minor work needed.
- The cell and spring have been designed and are being refined.

#### Main tasks to be completed:

- Finalise and produce cell and spring design. (3 weeks)
- Implement controllers on hardware. (5 weeks)
- Validate hardware results. (7 weeks)
- Complete dissertation. (9 weeks)
- All 2D work.

**Student name:** Theodore Abbott 15/03/2017  
**Supervisor:**

# List of Figures

1.1	Diagram comparing the path of a incident wave moving from a positive refractive index material (white) into another positive reactive index material (blue) or a negating refractive index metamaterial (yellow). . . . .	2
1.2	Diagram showing an example of how the system may look in two dimensions.	7
2.1	Diagram of the system to be modelled. . . . .	10
2.2	Diagram of the system to be emulated using the actively controlled system. . .	11
2.3	Graph showing the real component of the frequency response of the effective mass ( $m_{ep}$ ) and effective stiffness ( $k_{ep}$ ) of the passive system with simulation values of $m_t = 2\text{kg}$ , $m_a = 1\text{kg}$ , $c_a = 0.2\text{Nsm}^{-1}$ , $k_a = 1\text{Nm}^{-1}$ , $c_t = 2\text{Nsm}^{-1}$ and $k_t = 2\text{Nm}^{-1}$ . . . . .	15
2.4	Diagram showing the construction of the Precision Microdrives linear resonant actuator. Taken from Precision Microdrives promotional material. (2014) . .	17
2.5	Graphs showing the real components of the frequency response of the effective mass ( $m_e$ ) and effective stiffness ( $k_e$ ) of the system. $m_t = 2\text{kg}$ , $m_a = 1\text{kg}$ , $c_a = 0.2\text{Nsm}^{-1}$ , $k_a = 1\text{Nm}^{-1}$ , $c_t = 2\text{Nsm}^{-1}$ , $k_t = 2\text{Nm}^{-1}$ . The control gains were $g_m = -1$ and $g_k = -1$ . . . . .	18
3.1	Diagram showing the stripboard design for two LT1010 buffer amplifiers used to power the LRAs. . . . .	21
3.2	Picture of the Phidgets RB-Phi-203 100g Micro Load Cell. Modified from Phidgets promotional material and data sheet (2013). . . . .	22
3.3	<b>Left:</b> Stripboard design for two AD623 amplifiers used to amplify the signals from the load cells and accelerometers. <b>Right:</b> Operational amplifier diagram of the AD623 taken from the datasheet (2012). . . . .	23
3.4	Graphs showing the properties of materials considered for the transmission mass body. <b>Top:</b> Unfiltered graph of all material groups available in CES. <b>Bottom:</b> Filtered graph of plastics. . . . .	25
3.5	Initial design for the cell (white) including spring elements (grey). <b>Top right:</b> Top down view. <b>Bottom right:</b> Front view. . . . .	26
3.6	The first 3 prototype transmission mass bodies, oldest (left) to newest (right) (shown twice). . . . .	27
3.7	Image of a partially completed print showing the inner lattice between the faces of the shape. . . . .	27

3.8	<b>Left:</b> Several design iterations for the spring element from left (oldest) to right (newest). <b>Right:</b> The final spring element design attached to the transmission mass body by friction fit alone. . . . .	28
3.9	Problems encountered printing NinjaFlex on TAZ 4: <b>Left:</b> loss of accuracy due to small structure flexing while the head prints onto them. <b>Centre:</b> Object lifting off bed due to insufficient adhesion. <b>Right:</b> Very low quality printing on overhanging portions. Note that the inclusion of a brim around the base of the object prevents lifting off. . . . .	29
3.10	Best quality spring element print that was achieved with NinjaFlex. . . . .	31
3.11	Redesign of the transmission mass body. . . . .	32
3.12	<b>Top:</b> Technical drawing of the redesigned transmission mass body. <b>Bottom:</b> Adapted transmission mass body for end cell with mounting point for load cell. . . . .	33
3.13	Strain simulations of the transmission mass body designs. <b>Top:</b> Simplest minimum functional design required for using NinjaFlex. <b>Bottom:</b> Final design. . . . .	34
3.14	Assembled end cell. <b>Left:</b> Exploded View. <b>Right:</b> Fully assembled. . . . .	35
3.15	The PTFE plate and plywood base. . . . .	35
3.16	Full 1D assembly of 3 cells on the PTFE base. Accelerometers are shown in green and the LRAs are the small silver cylinders inside the transmission mass bodies. . . . .	36
3.17	Technical drawing of full 1D assembly of 3 cells on the PTFE base. . . . .	37
3.18	Graphs showing the simulated real components of the frequency response of the effective mass ( $m_e$ ) and effective stiffness ( $k_e$ ) for the real parameters of the active and passive system. . . . .	39
4.1	Experimental setup used for capturing data. . . . .	42
4.2	Example of the time history of the accelerometer and load cell signals generated experimentally. . . . .	43
4.3	Lumped model of massive spring. . . . .	44
4.4	Experimental results for the transmission only and full passive system. . . . .	45
4.5	Experimental results for the passive system and the active system with both positive and negative gains. It is clear that the negative gain produces a deeper and wider resonant trough. . . . .	47
4.6	Experimental results for the actively controlled system at various gains. . . . .	48
5.1	Gantt chart indicating progress against the planned work program. . . . .	

# Bibliography

- Akl, W. & Baz, a. (2013), 'Active acoustic metamaterial with simultaneously programmable density and bulk modulus', *Journal of Vibration and Acoustics* **135**(June), 31001.  
**URL:** <http://dx.doi.org/10.1115/1.4023141>
- Akl, W. & Baz, a. (n.d.), 'Multi-cell Active Acoustic Metamaterial with Programmable Bulk Modulus', *Journal of Intelligent Material Systems and Structures* (5), 541–556.  
**URL:** <http://jim.sagepub.com> <http://www.sagepub.co.uk/journalsPermissions.nav>, volume = 21, year = 2010
- Baz, A. (2009), 'The structure of an active acoustic metamaterial with tunable effective density', *New Journal of Physics* **11**.
- Daley, S. A. P., Laalej, H. & S (2012), 'Performance and stability analysis of active elastic metamaterials with a tunable double negative response', *Smart Materials and Structures* **21**(12), 125021.  
**URL:** <http://stacks.iop.org/0964-1726/21/i=12/a=125021>
- Devices, A. (2012), 'Low Cost Instrumentation Amplifier AD622 \* Product Page Quick Links', *AD623 Datasheet* .  
**URL:** <http://www.analog.com/en/products/amplifiers/instrumentation-amplifiers/ad623.html>
- Deza, M. & Shtogrin, M. (2000), 'Uniform Partitions of 3-space, their Relatives and Embedding', *European Journal of Combinatorics* **21**(6), 807–814.  
**URL:** <http://www.sciencedirect.com/science/article/pii/S0195669899903852>
- Duan, Z., Wu, B. I., Lu, J., Au Kong, J. & Chen, M. (2008), 'Reversed Cherenkov radiation in a waveguide filled with anisotropic double-negative metamaterials', *Journal of Applied Physics* **104**(6).
- Ge, L., Sethi, S., Ci, L., Ajayan, P. M. & Dhinojwala, A. (2007), 'Carbon nanotube-based synthetic gecko tapes.', *Proceedings of the National Academy of Sciences of the United States of America* **104**(26), 10792–10795.
- Hales, T. C. (2001), 'The Honeycomb Conjecture', *Discrete and Computational Geometry* **25**(1), 122.  
**URL:** <http://link.springer.com/article/10.1007%2Fs004540010071>

- Lai, Y., Wu, Y., Sheng, P. & Zhang, Z.-Q. (n.d.), ‘Hybrid elastic solids.’, *Nature Materials* (8), 620–624.  
**URL:** <http://dx.doi.org/10.1038/nmat3043>, volume = 10, year = 2011
- Lassiter, J. B. & Halas, N. J. (2012), ‘Complex Plasmonic Nanostructures: Symmetry Breaking and Coupled Systems’, *Physics and Astronomy Doctor of*, 108.
- Liu, X. N., Hu, G. K., Huang, G. L. & Sun, C. T. (2011), ‘An elastic metamaterial with simultaneously negative mass density and bulk modulus’, *Applied Physics Letters* **98**(25), 2–4.
- McEvoy, M. A. & Correll, N. (2015), ‘Materials that couple sensing, actuation, computation, and communication’, *Science* **347**(6228), 1261689–1261689.  
**URL:** <http://www.sciencemag.org/content/347/6228/1261689.abstract>
- Microdrives, P. (2014), ‘C08-001 Product Data Sheet Precision Haptic™ Model : C08-001 C08-001 Understanding Precision Microdrives Specification and Production Stages’, **44**(0), 1–5.
- Pelegrinis, M. T., Pope, S. A. & Daley, S. (2012), ‘Acoustic Impedance Matching using Loop Shaping PID Controller Design’.
- Popa, B. I., Zigoneanu, L. & Cummer, S. A. (2013), ‘Tunable active acoustic metamaterials’, *Physical Review B - Condensed Matter and Materials Physics* **88**(2).
- Pope, S. A. (2013), ‘Double negative elastic metamaterial design through electrical-mechanical circuit analogies’, *IEEE Transactions on Ultrasonics, Ferroelectrics, and Frequency Control* **60**(7), 1467–1474.
- Pope, S. A. & Daley, S. (2010), ‘Viscoelastic locally resonant double negative metamaterials with controllable effective density and elasticity’, *Physics Letters, Section A: General, Atomic and Solid State Physics* **374**(41), 4250–4255.  
**URL:** <http://dx.doi.org/10.1016/j.physleta.2010.08.037>
- Pope, S. a. & Laalej, H. (2014), ‘A multi-layer active elastic metamaterial with tuneable and simultaneously negative mass and stiffness’, *Smart Materials and Structures* **23**(7), 075020.
- Pope, S. A., Laalej, H. & Kadirkamanathan, V. (2014), ‘An Experimental Analysis of an Active Elastic Metamaterial’.
- Pope, S. A., Pelegrinis, M. & Daley, S. (2011), ‘A consideration of impedance matching issues with Metamaterials’, *Proceeding of Internoise 2011* pp. 1–8.
- Ubaid, U., Daley, S. & Pope, S. A. (2015), ‘Design of remotely located and multi-loop vibration controllers using a sequential loop closing approach’.
- Wedel, M. J. (2005), ‘Postcranial Skeletal Pneumaticity in Sauropods and Its Implications for Mass Estimates’, *The Sauropods: Evolution and Paleobiology* pp. 201–228.  
**URL:** <http://sauroposeidon.files.wordpress.com/2010/04/wedel-2005-mass-estimates.pdf>

Wee, W. H. & Pendry, J. B. (2010), 'Looking beyond the perfect lens', *New Journal of Physics* **12**.

Wegener, M. (2013), 'Metamaterials beyond optics', *Science* **342**(6161), 939–940.

**URL:** <http://www.sciencemag.org/content/342/6161/939.short>

Zhang, S., Yin, L. & Fang, N. (2009), 'Focusing ultrasound with an acoustic metamaterial network', *Physical Review Letters* **102**(19), 1–4.